

Nanoscale magnetic resonance spectroscopy using a carbon nanotube double quantum dot

Wanlu Song,^{1,2,*} Tianyi Du,^{1,*} Haibin Liu,^{1,2,†} Martin B. Plenio,^{3,2} and Jianming Cai^{1,2,‡}

¹*School of Physics, Huazhong University of Science and Technology, Wuhan 430074, China*

²*International Joint Laboratory on Quantum Sensing and Quantum Metrology,
Huazhong University of Science and Technology, Wuhan, 430074, China*

³*Institut für Theoretische Physik & IQST, Albert-Einstein Allee 11, Universität Ulm, D-89081 Ulm, Germany*

(Dated: December 14, 2021)

Quantum sensing exploits fundamental features of quantum mechanics and quantum control to realise sensing devices with potential applications in a broad range of scientific fields ranging from basic science to applied technology. The ultimate goal are devices that combine unprecedented sensitivity with excellent spatial resolution. Here, we propose a new platform for all-electric nanoscale quantum sensing based on a carbon nanotube double quantum dot. Our analysis demonstrates that the platform can achieve sensitivities that allow for the implementation of single-molecule magnetic resonance spectroscopy and therefore opens a promising route towards integrated on-chip quantum sensing devices.

I. INTRODUCTION

Quantum systems embodying fundamental quantum features offer an appealing perspective in sensing and metrology [1–4]. Ultra-small quantum sensors provide the possibility for locating them in very close proximity to the target to realise strong sensor-target interaction. This facilitates sensing with both ultra-high measurement sensitivity combined with a nanoscale resolution thus allowing for the identification of nanoscale objects or the detection of signals carrying, for example, magnetic information of nano-structures. The thereof emerging technology of nanoscale magnetic resonance spectroscopy provides a versatile experimental tool to investigate a wide range of physical, chemical and biophysical phenomena in minute sample volumes [5–14].

There are two key challenges for the implementation of nanoscale magnetic resonance spectroscopy. First, the smallest possible probe-target distance is generally limited by the size of the quantum sensor. Remarkably, nanoscale quantum sensors based on nitrogen-vacancy (NV) center in diamond [15–17] can achieve sizes of a few nanometers. However, perturbations from the surface then start to significantly affect its sensing capabilities thus limiting further miniaturisation [18–21]. Secondly, a scalable architecture of an integrated on-chip quantum sensing device would represent fundamental progress in the development of nanoscale magnetic resonance spectroscopy with appealing practical applications.

In this work, we address both challenges and propose a new type of quantum sensor based on a valley-spin qubit of a carbon nanotube double quantum dot [22–29] aiming for on-chip nanoscale magnetic resonance spectroscopy. By applying continuous electrical driving on a double quantum dot, the system can efficiently identify the frequency of weak external signals. Due to the nanometer diameter of single walled carbon nanotubes, the valley-spin quantum sensor can be brought extremely close to the target which promises ultra-high sen-

sitivity. Our detailed analysis based on realistic experimental parameters demonstrates that such a carbon nanotube quantum sensor is able to identify the species of individual external nuclei, thus going well beyond both the detection of external ensembles of nuclei [30] and the detection of a single strongly coupled intrinsic nucleus [31], and thereby provides a new platform for nanoscale magnetic resonance spectroscopy. The system can be controlled coherently [32, 33] and efficiently readout [34, 35] electrically. Such all-electric manipulation without requiring optical elements facilitates the integration of on-chip carbon nanotube quantum sensor arrays [36]. The present result is expected to extend the scope of quantum technologies based on a carbon nanotube double quantum dot system from quantum information processing to nanoscale magnetic resonance spectroscopy.

II. MODEL OF A NANOTUBE QUANTUM SENSOR

Our quantum sensor is based on a carbon nanotube double quantum dot, as shown in Fig. 1(a). In a single-wall carbon nanotube, an electron has two angular momentum quantum numbers, arising from spin and orbital motions. The orbital motion has two flavours known as the K and K' valleys, which correspond to the clockwise and counterclockwise motions around the nanotube. Due to the anisotropy of orbital magnetic moment [37], the energy levels of electron in carbon nanotube become sensitive to the direction of a magnetic field, which has been applied into the detection of static magnetic fields [38, 39] and electrically driven electron spin resonance [32, 33]. Although it has been demonstrated that nuclear magnetic fields may influence electron transport [35] and electron spin resonance [30] in a double quantum dot confined in the GaAs heterostructure, it is not clear how the mechanism can be engineered for nanoscale magnetic resonance spectroscopy.

The goal of the present work is to design a quantum sensor based on a carbon nanotube double quantum dot system that can achieve a sensitivity on the order of $10 \text{ nT}/\sqrt{\text{Hz}}$ for weak oscillating magnetic fields, which is sufficient for achieving nuclear magnetic resonance spectroscopy at the single-molecule level. The key idea which enables us to achieve such a goal

* These authors contributed equally.

† liuhb@hust.edu.cn

‡ jianmingcai@hust.edu.cn

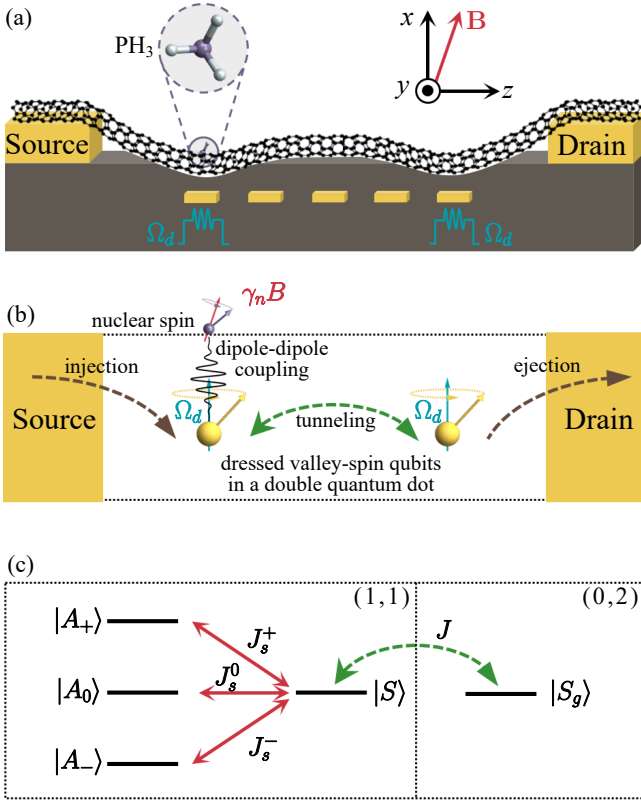


Fig.1. A nanotube quantum sensor for nanoscale magnetic resonance spectroscopy. (a) Model of a (bent) nanotube quantum sensor for nanoscale magnetic resonance spectroscopy (a PH₃ molecule shown as an illustrative example). Five local gate electrodes create an electrically driven double quantum dot and control the electron tunneling rates [32, 33]. (b) shows the mechanism of a nanotube quantum sensor. Both electrons are electrically driven with a Rabi frequency Ω_d , the magnetic dipole-dipole coupling between one electron spin and the external target spin (with a Larmor frequency $\gamma_n B$) will lift the Pauli blockade, see (c), and lead to a resonant leakage current when $\Omega_d = \gamma_n B$. (c) Due to a change in the local environment of the left or right quantum dot, Pauli blockade is lifted by three additional tunnelling channels as denoted by $|A_{0,\pm}\rangle \leftrightarrow |S\rangle \leftrightarrow |S_g\rangle$ with the corresponding tunneling rates $J_s^{0,\pm}$ and J .

is continuous electrical driving on a carbon nanotube double quantum dot which leads to resonant leakage current when the driving Rabi frequency matches the fingerprint frequency of a weak signal (e.g. arising from nuclei), see Fig.1(b-c). This in turn allows to obtain the relevant information on the weak signal from the electron transport spectroscopy in Pauli blockade regime [27].

In a static magnetic field B , the Hamiltonian of an electron in nanotube is given by (for simplicity we set $\hbar = 1$) [32, 40]

$$\hat{H}(z) = -\frac{1}{2}\Delta_{SO}\hat{\tau}_3\mathbf{n}(z) \cdot \hat{\boldsymbol{\sigma}} - \frac{1}{2}\Delta_{KK'}(\hat{\tau}_1 \cos \varphi + \hat{\tau}_2 \sin \varphi) + \frac{1}{2}g_s\mu_B\mathbf{B} \cdot \hat{\boldsymbol{\sigma}} + g_{orb}\mu_B\mathbf{B} \cdot \mathbf{n}(z)\hat{\tau}_3, \quad (1)$$

where $\hat{\boldsymbol{\tau}} = (\hat{\tau}_1, \hat{\tau}_2, \hat{\tau}_3)$ and $\hat{\boldsymbol{\sigma}} = (\hat{\sigma}_x, \hat{\sigma}_y, \hat{\sigma}_z)$ are the Pauli operators of valley and spin, $\mathbf{n}(z) = \cos \theta(z)\hat{z} + \sin \theta(z)\hat{x}$

is the local tangent unit vector with $\theta(z)$ the angle between $\mathbf{n}(z)$ and \hat{z} , Δ_{SO} is the spin-orbit coupling strength [41], $\Delta_{KK'}$ and φ are the magnitude and phase of valley mixing [42], g_s and g_{orb} are the g factors of spin and valley respectively. At $\theta(z_0) = 0$ and $B = 0$, four eigenstates form two Kramers doublets $\{|\uparrow^*\rangle, |\downarrow^*\rangle\}$ and $\{|\uparrow\rangle, |\downarrow\rangle\}$ which are separated by an energy gap $\Delta E_0 = (\Delta_{SO}^2 + \Delta_{KK'}^2)^{1/2}$. Each doublet can serve as a valley-spin qubit which shows different energy splittings in the parallel ($B = B_z\hat{z}$) and perpendicular ($B = B_x\hat{x}$) magnetic field due to the anisotropic magnetic moment. As mediated by a bent nanotube [43], the qubit can be electrically driven while the quantum dot is driven back and forth with frequency ω and amplitude Δz_m by applying a microwave frequency gate voltage.

The effective Hamiltonian of a driven valley-spin qubit in the magnetic field $B = \{B_x, 0, B_z\}$ is [40] $\hat{H}_e = \frac{1}{2}(\omega_x\hat{s}_x + \omega_z\hat{s}_z) + \Omega_x \cos(\omega t)\hat{s}_x + \Omega_z \cos(\omega t)\hat{s}_z$, where $\hat{s}_{x,y,z}$ are Pauli operators of the valley-spin qubit and $\omega_x = g_\perp\mu_B B_x$, $\omega_z = g_\parallel\mu_B B_z$, with $g_\perp = g_s \sin \zeta$, $g_\parallel = g_s - 2ag_{orb} \cos \zeta$. The characteristic parameter ζ is defined as $\tan \zeta = \Delta_{KK'}/\Delta_{SO}$, and a takes the value ± 1 for the upper and lower Kramers doublets respectively. We choose $\omega = \omega_0 \equiv (\omega_x^2 + \omega_z^2)^{1/2}$ and obtain a dressed valley-spin qubit under the conditions $\Omega_x, \Omega_z \ll \omega_0$ as described by (see more details in Appendix A)

$$\hat{H}_d = \frac{1}{2}\Omega_d\hat{S}_x \quad (2)$$

where \hat{S}_x is Pauli operator in the eigenbasis of $\hat{H}_0 = (1/2)(\omega_x\hat{s}_x + \omega_z\hat{s}_z)$ and the driving Rabi frequency is $\Omega_d = \Omega_x \cos \gamma - \Omega_z \sin \gamma$ with $\tan \gamma = \omega_x/\omega_z$. Note that the effect of fluctuation in the driving fields can be mitigated by concatenated driving schemes [44].

We consider a double quantum dot in the n - p region and encode a valley-spin qubit in the lower Kramers doublet for both quantum dots. In the Pauli blockade regime, electron tunneling is forbidden when two electrons in the (1, 1) configuration are in a triplet state [45]. The leakage current can be obtained from the quantum transport master equation (see more details in Appendix B). When the Rabi frequency of an applied continuous driving field on the valley-spin qubits matches the frequency of local signal fields, e.g. from the hyperfine coupling between left quantum dot and a single molecule, additional electron tunnelling channels open up, see Fig.1(c). In the following, we show that the change in the leakage current through such a nanotube quantum dot system can serve as a highly sensitive probe for selective detection of localised external signals.

III. SENSING OF A WEAK OSCILLATING FIELD

To illustrate the working principle of nanoscale magnetic resonance spectroscopy using a nanotube quantum sensor, we first consider the measurement of an oscillating magnetic field (e.g. arising from a local magnetic moment) $\mathbf{b}(t) = b \cos(\omega_c t)\hat{z}$ acting on left quantum dot, where the right quantum dot is out of the nanoscale field due to the much larger distance from the left quantum dot. The effective

Hamiltonian in the (1, 1) subspace is

$$\hat{H}_{sb} = \frac{1}{2}\Omega_d\hat{S}_x^{(1)} + \Omega_c \cos(\omega_c t)\hat{S}_z^{(1)} + \frac{1}{2}\Omega_d\hat{S}_x^{(2)}, \quad (3)$$

where $\hat{S}_{x,z}^{(j)}$ are the Pauli operators of left ($j = 1$) and right ($j = 2$) dressed valley-spin qubit, and $\Omega_c = g_{\parallel}\mu_B b/2$ represents the coupling strength of left dressed valley-spin qubit to the weak oscillating magnetic field. The Hamiltonian in the (0, 2) subspace is $H_{\Delta} = \Delta|S_g\rangle\langle S_g|$ with the energy detuning Δ , and the tunnelling Hamiltonian is $H_t = J(|S\rangle\langle S_g| + |S_g\rangle\langle S|)$. In the new picture after making a transformation $\hat{S}_x \leftrightarrow \hat{S}_z$ and using rotating wave approximation, we introduce the basis states including

$$|A_0\rangle = \frac{1}{\sqrt{2}} \begin{pmatrix} \cos \vartheta \\ \sin \vartheta \\ \sin \vartheta \\ -\cos \vartheta \end{pmatrix}, \quad |A_{\pm}\rangle = \frac{1}{2} \begin{pmatrix} \pm 1 + \sin \vartheta \\ -\cos \vartheta \\ -\cos \vartheta \\ \pm 1 - \sin \vartheta \end{pmatrix} \quad (4)$$

and the singlet state $|S\rangle = (1/\sqrt{2}) \begin{pmatrix} 0 & -1 & 1 & 0 \end{pmatrix}^T$ with $\cos \vartheta = \Omega_c/\lambda$, $\sin \vartheta = 2\delta/\lambda$, $\delta = \Omega_d - \omega_c$ and $\lambda = (4\delta^2 + \Omega_c^2)^{1/2}$, to rewrite the Hamiltonian \hat{H}_{sb} as

$$\hat{H}_{sb}'' = \begin{pmatrix} 0 & 0 & 0 & J_S^0 \\ 0 & \lambda/2 & 0 & J_S^+ \\ 0 & 0 & -\lambda/2 & J_S^- \\ J_S^0 & J_S^+ & J_S^- & 0 \end{pmatrix}, \quad (5)$$

where the local field induced tunneling rates are $J_S^0 = -\Omega_c^2/(2\lambda)$ and $J_S^+ = J_S^- = \delta\Omega_c/(\sqrt{2}\lambda)$ (see more details in Appendix B).

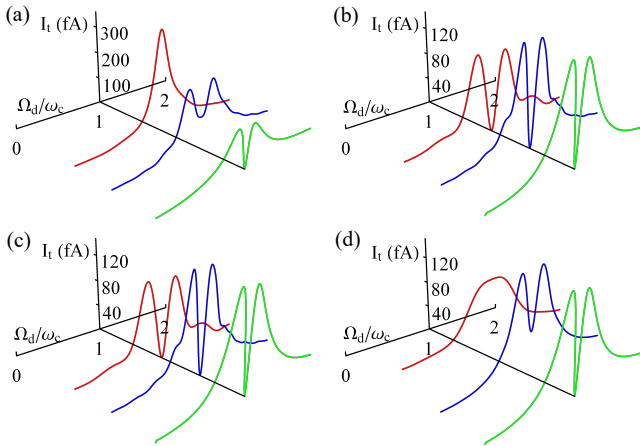


Fig.2. Illustration of quantum sensing mechanism. (a)-(d) Leakage current I_t as a function of the driving Rabi frequency Ω_d/ω_c with the initial state $|A_0\rangle$ (a), $|A_+\rangle$ (b), $|A_-\rangle$ (c) and the unpolarized electron spin state (d) in (0, 1) subspace at time $t = 0.5 \mu\text{s}$ (red), $1 \mu\text{s}$ (blue), $10 \mu\text{s}$ (green) respectively. The parameters are $g_{orb} = 12$, $\Delta_{SO} = 0.8 \text{ meV}$, $\Delta_{KK'} = 0.2 \text{ meV}$, $\varphi = 0$ for both electrons [33, 40], and $\omega_c = (2\pi) 5 \text{ MHz}$, $b = 6 \mu\text{T}$ for the oscillating signal field, the electron injection and ejection rate are $\Gamma_L = \Gamma_R = (2\pi) 8 \text{ MHz}$ and the tunneling rate is $J = (2\pi) 2 \text{ MHz}$.

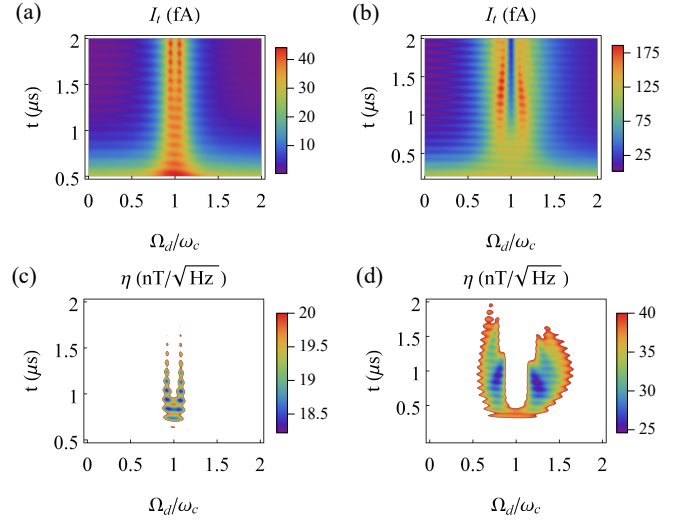


Fig.3. Performance of measurement sensitivity. (a)-(b) Leakage current I_t and (c)-(d) estimated sensitivity η (at the resonant peaks and dip of leakage current) as a function of the driving Rabi frequency Ω_d/ω_c and the evolution time t for an oscillating magnetic field with different amplitudes: (a, c) $b = 2 \mu\text{T}$ and (b, d) $b = 6 \mu\text{T}$. The system starts from one unpolarised electron located in the right quantum dot as the initial state. The other parameters are the same as Fig.2.

The above Hamiltonian reveals two essential ingredients of the present nanotube quantum sensor. Firstly, in the absence of an oscillating magnetic field, all of the channels to the state $|S\rangle$ are closed, and the leakage current is only contributed by the state $|S\rangle$. The external oscillating field opens up three additional channels $|A_{0,\pm}\rangle \leftrightarrow |S\rangle \leftrightarrow |S_g\rangle$ for electron tunnelling, see Fig.1(c), and thus can significantly influence the leakage current. Secondly, the transition $|A_0\rangle \leftrightarrow |S\rangle$ is most efficient when $\Omega_d = \omega_c$, as shown in Fig.2(a). In contrast, the transitions $|A_{\pm}\rangle \leftrightarrow |S\rangle$ play a most significant role with a slight detuning between Ω_d and ω_c , which is verified by the resonant dip of leakage current in Fig.2(b)-(c). As the electron injected from the source is unpolarised, the total leakage current reflects an overall contribution of all tunnelling channels. As the system evolves, the transitions $|A_{\pm}\rangle \leftrightarrow |S\rangle$ becomes dominant, which leads to a pronounced resonant dip as evident in Fig.2(d). These features demonstrate the feasibility of using such a nanotube quantum sensor to selectively detect a weak oscillating magnetic field from driving field induced variations in the leakage current.

By sweeping the Rabi frequency Ω_d of the driving field, a resonance appears in the leakage current when it matches the frequency of the weak oscillating magnetic field emanating from the target (i.e. $\Omega_d = \omega_c$), as shown in Fig.3(a-b). Such a resonance measurement offers an efficient way to identify the frequency of the external signal, which provides a basis for single-molecule nuclear magnetic resonance spectroscopy. We further analyse the shot-noise limited sensitivity for the measurement of the amplitude of a weak oscillating field from the instantaneous leakage current I at time t , which is defined by $\eta = \Delta I \sqrt{t} (\partial_b I)^{-1}$. We estimate the achievable sensitivity from the measurement of the resonant leakage current in the

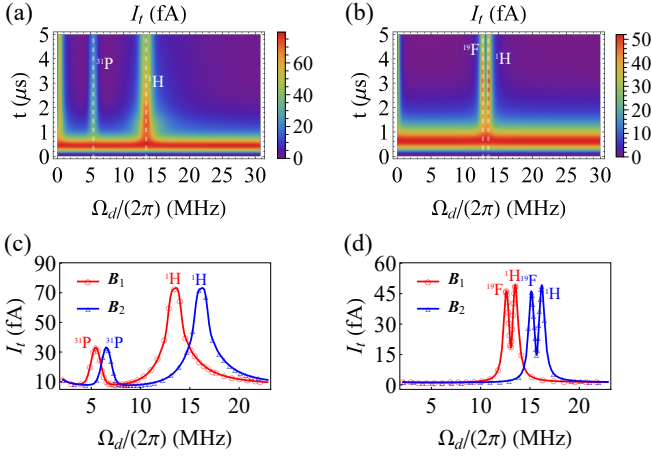


Fig.4. Single-molecule magnetic resonance spectroscopy. (a)-(b) Leakage current I_t as a function of the driving Rabi frequency Ω_d and the evolution time t for the detection of a single PH_3 molecule with $\Gamma_L = (2\pi) 1$ MHz, $\Gamma_R = (2\pi) 0.6$ MHz, $J = (2\pi) 0.55$ MHz (a) and a single HF molecule with $\Gamma_L = (2\pi) 1$ MHz, $\Gamma_R = (2\pi) 0.4$ MHz, $J = (2\pi) 0.35$ MHz (b) in the magnetic field $B = \{300, 0, 100\}$ mT. The dash lines (white) in (a)-(b) represents the corresponding Larmor frequencies. (c)-(d) Leakage current I_t as a function of the driving Rabi frequency Ω_d at time $t = 1.5 \mu\text{s}$ for the detection of a single PH_3 molecule (c) and at time $t = 3 \mu\text{s}$ for the detection of a single HF molecule (d) in different magnetic fields with $B_1 = \{300, 0, 100\}$ mT and $B_2 = \{360, 0, 120\}$ mT. The other parameters are the same as Fig.2.

weak field regime as shown in Fig.3(c-d), which implies that the sensitivity can reach the order of $10 \text{ nT}/\sqrt{\text{Hz}}$ by measuring the instantaneous leakage current after an evolution time of a few microseconds using the feasible experimental parameters given in Fig.2.

IV. NANOSCALE MAGNETIC RESONANCE SPECTROSCOPY

Based on the idea presented and analysed above in the scenario of measuring a weak oscillating signal field, we proceed to demonstrate the applicability of the present scheme for nanoscale magnetic resonance spectroscopy at a single-molecule level. Without loss of generality, we assume that a target molecule is attached on the surface of the nanotube close to the left quantum dot. The interaction strength of magnetic dipole-dipole coupling between the nuclear spins of the target molecule and the valley-spin qubit is $h_n = \mu_0 \mu_B \mu_N g_n g_{\parallel} / (4\pi r^3)$ where r represents the distance from the valley-spin qubit and individual nuclear spins. Two unique features of the present proposal are responsible for its excellent performance, namely a large value of g_{\parallel} (due to a much more prominent orbital g -factor g_{orb}) and the achievable small sensor-target distance r (which benefits from the compact dimension of nanotube).

A single molecule is characterized by different species of nuclear spins with multiple Larmor frequencies. For each

nuclear spin, an effective magnetic field introduced by its Larmor precession influences the energy levels of left quantum dot through the magnetic dipole-dipole coupling. It leads to individual resonance signals of leakage current that are detected by the present driven nanotube quantum sensor. The identification of these characteristic Larmor frequencies, as implemented by sweeping the Rabi frequency of continuous driving, provides a fingerprint for the detection of single molecules. As an example, we consider phosphine (PH_3) and hydrogen fluoride (HF) molecule, both of which are toxic gases. As shown in Fig.4, owing to the half-integer nuclear spins ^1H , ^{19}F and ^{31}P , the leakage current clearly exhibits resonances when the Rabi frequency of continuous driving matches the condition $\Omega_d = \gamma_n B$, where γ_n is the gyromagnetic ratio corresponding to individual nuclear species. We remark that electron injection (ejection) rates and the tunneling rate can be tuned by local gate voltages in order to optimize the performance of the protocol (see more details in Appendix D).

V. FEASIBILITY OF EXPERIMENTAL REALISATION

Current experimental advances in fabricating nanotube quantum dot and electrically driven spin resonance quantum control facilitates the implementation of our proposed scheme. The key ingredient for experimental realization is the tuneable Rabi frequency of electric continuous driving Ω_d . The driving Rabi frequency depends on the bending parameter $(\partial_z \theta)_{z=z_0}$ and the oscillation amplitude Δz_m of the quantum dot, the required value of which is feasible with the state-of-the-art experiment capability [33, 40]. The scheme prefers two valley-spin qubits that have the same valley mixing $\Delta_{KK}^{(j)}$, thereby the same characteristic parameter ζ_j for two valley-spin qubits. In order to compensate for non-uniformity in quantum dots and achieve the best sensing performance, we adopt a bent arc shape nanotube with an appropriate tilted angle. By applying a magnetic field in \hat{x} - \hat{z} plane with the proper components of B_x , B_z , we find that two valley-spin qubits can have identical parameters ζ_j (see more details in Appendix B).

The main decoherence that may affect the performance of the present carbon nanotube quantum sensor arises from the thermal phonons, the environmental nuclear spins and the charge fluctuation. At low temperature $T = 100$ K, the dominated bending-mode phonon-mediated spin relaxation time is about $1 \mu\text{s}$ [46], which is much longer than the electron tunnelling time in quantum dot. The influence of nuclei may be mitigated by synthesizing carbon nanotube with isotopically purified $^{12}\text{CH}_4$, allowing for the fabrication of almost nuclei-spin-free devices [22, 47, 48]. In addition, the driving via continuous control fields serves to suppress noise effects from nuclear impurities in the device, which underlines their importance in our scheme. Our numerical simulation shows that the performance is robust given feasible isotopic engineering (see more details in Appendix C). As the carbon nanotube quantum dot is gate-defined, the charge noise would modify the energy levels of the quantum dot, i.e., inducing fluctuations of the energy detuning Δ between the singlet states $|S\rangle$ and $|S_g\rangle$ [39], the role of which in our scheme is mainly the suppression

of effective tunneling. The charge noise is slow [49] and its influence can be compensated by optimizing the parameters Γ_L , Γ_R and J to sustain the leakage current (see more details in Appendix C). We stress that this is quite different from the dephasing effect on the coherence time of qubit involving the singlet state $|S_g\rangle$ in the (0,2) subspace [33], where the energy splitting of the qubit relies on the energy detuning Δ .

We note that the higher-order tunneling (cotunneling) processes [50, 51] may also have influence on our scheme. As the cotunneling corrections $\propto \Gamma_L \Gamma_R$ [50, 52], it is helpful to make the tunnel rates small for the suppression of cotunneling current. In our scheme, the tunnel rates Γ_L, Γ_R are 1 ~ 2 orders of magnitude smaller than the values in Ref.[51], thus the cotunneling current here is estimated to be much less than 3 fA, which would not significantly influence the performance of our scheme. Overall, we remark that the implementation of our proposal may require new experimental efforts, the feasibility of which appears promising.

VI. CONCLUSIONS & OUTLOOK

To summarise, we propose a new platform for nanoscale magnetic resonance spectroscopy using a continuously driven carbon nanotube double quantum dot as a quantum sensor. The system allows to achieve a high sensitivity due to its unique features of a large valley g -factor and ultra-small dimension. In particular, our simulation demonstrates that such a quantum sensor may identify individual nuclear spin and detect a single molecule. The all-electric control and readout techniques make it appealing for on-chip quantum sensing device integration. Assisted by the functionalized carbon nanotube [53, 54], such a quantum sensor can serve as a nanoscale probe to capture the target molecule selectively and provide a new route to implement nanoscale magnetic resonance spectroscopy at a single-molecule level with a wide range of potential applications both in basic science and applied technology.

ACKNOWLEDGMENTS

We thank Ying Li, Guido Burkard and Andras Palyi for valuable discussions and suggestions. The work is supported by National Natural Science Foundation of China (11874024, 11574103, 11690030, 11690032). W.S. is supported by the Postdoctoral Innovation Talent Program, H.L. is also supported by the China Postdoctoral Science Foundation grant (2016M602274). M.B.P. is supported by the EU projects ASTERIQS and HYPERDIAMOND, the ERC Synergy grant BioQ and the BMBF via DiaPol and NanoSpin.

Appendix A: Derivation of effective Hamiltonian

Electrons in a nanotube have two angular momentum quantum numbers, arising from the spin and the valley degree of freedom. These two degrees of freedom are coupled via spin-orbit interaction [41]. In addition, two valley states are coupled

to each other by electrical disorder and contact electrodes [42]. We introduce the identity and Pauli matrices in the spin space $\hat{\sigma}_i$ with $i = \{0, x, y, z\}$ and the three-dimensional spin vector $\hat{\sigma} \equiv \{\hat{\sigma}_x, \hat{\sigma}_y, \hat{\sigma}_z\}$. The positive and negative projections of $\hat{\sigma}_z$ (component of $\hat{\sigma}$ along \hat{z} -axis) are denoted by $\{|\uparrow\rangle, |\downarrow\rangle\}$. Similarly, the identity and Pauli matrices in the valley space are denoted as $\hat{\tau}_j$ with $j = \{0, 1, 2, 3\}$ and the three-dimensional valley vector $\hat{\tau} \equiv \{\hat{\tau}_1, \hat{\tau}_2, \hat{\tau}_3\}$, where we choose $\{|K'\rangle, |K\rangle\}$ as the positive and negative projections of $\hat{\tau}_3$ (component of $\hat{\tau}$ along $\mathbf{n}(z) = \cos \theta(z) \mathbf{z} + \sin \theta(z) \mathbf{x}$ which is a local tangent unit vector of the nanotube with $\theta(z)$ the angle between $\mathbf{n}(z)$ and \mathbf{z}). In a static magnetic field \mathbf{B} , the Hamiltonian of an electron can be written as [32, 40]

$$\hat{H} = -\frac{1}{2}\Delta_{SO}\hat{\tau}_3\mathbf{n}(z) \cdot \hat{\sigma} - \frac{1}{2}\Delta_{KK'}(\hat{\tau}_1 \cos \varphi + \hat{\tau}_2 \sin \varphi) + \frac{1}{2}g_s\mu_B\mathbf{B} \cdot \hat{\sigma} + g_{orb}\mu_B\mathbf{B} \cdot \mathbf{n}(z) \hat{\tau}_3, \quad (\text{A1})$$

where Δ_{SO} is the spin-orbit coupling strength, $\Delta_{KK'}$ and φ are the magnitude and phase of valley mixing, g_s and g_{orb} are the spin and orbital g factors respectively. We remark that g_{orb} is much larger than g_s , and would provide an advantage for magnetic field sensing [39]. At $\theta(z_0) = 0$ and $\mathbf{B} = 0$, four eigenstates are separated by an energy gap $\Delta E_0 = (\Delta_{SO}^2 + \Delta_{KK'}^2)^{1/2}$ and form two Kramers doublets $\{|\uparrow^*\rangle, |\downarrow^*\rangle\}$ and $\{|\uparrow\rangle, |\downarrow\rangle\}$ with

$$|\uparrow^*\rangle = -\cos(\zeta/2)|K'\rangle|\downarrow\rangle + \sin(\zeta/2)|K\rangle|\downarrow\rangle, \quad (\text{A2})$$

$$|\downarrow^*\rangle = -\sin(\zeta/2)|K'\rangle|\uparrow\rangle + \cos(\zeta/2)|K\rangle|\uparrow\rangle, \quad (\text{A3})$$

$$|\uparrow\rangle = \cos(\zeta/2)|K'\rangle|\uparrow\rangle + \sin(\zeta/2)|K\rangle|\uparrow\rangle, \quad (\text{A4})$$

$$|\downarrow\rangle = \sin(\zeta/2)|K'\rangle|\downarrow\rangle + \cos(\zeta/2)|K\rangle|\downarrow\rangle, \quad (\text{A5})$$

with $\tan \zeta = \Delta_{KK'}/\Delta_{SO}$ (without loss of generality we consider $\varphi = 0$), either of which can serve as a valley-spin qubit.

Electrons in nanotube can be longitudinally confined to form a quantum dot by introducing tunnel barriers which can be created by modifying the electrostatic potential with gate voltages. For a double quantum dot, even the tunnelling of a single electron is permitted by Coulomb blockade, the transition from a ground (1,1)-triplet state with one electron in each dot to a ground (0,2)-singlet state with both electrons in the right dot is blocked by Pauli exclusion principle, hence the leakage current is zero. In carbon nanotube, the energy difference between an excited (0,2)-triplet state and a ground (0,2)-singlet state can be one or two orders of magnitude smaller than in III-V materials, which gives rise to the transition from a ground (1,1)-triplet state to an excited (0,2)-triplet state, hence the Pauli blockade does not work perfectly. A robust Pauli blockade in carbon nanotube is most evident with a double quantum dot tuned into the n-p region, where the first shells of electrons and holes are separated by a large gap [27].

Based on Pauli blockade in a double quantum dot, we consider two valley-spin qubits both of which are encoded in the lower Kramers doublet $\{|\uparrow^*\rangle, |\downarrow^*\rangle\}$, then the leakage current can be regarded as a *meter* of the right valley-spin qubit and the left valley-spin qubit servers as a quantum *probe* interacting with a target. In our scheme, two dressed valley-spin qubits in

a double quantum dot can be used as a nanotube quantum sensor to detect e.g. a local magnetic field or a locally interacting spin.

1. Dressed valley-spin qubit

A valley-spin qubit in a static magnetic field B can be electrically driven when the quantum dot in a bent nanotube is driven by an microwave gate voltage [32, 33]. We denote the frequency and the amplitude of the driven motion of the quantum dot as ω and Δz_m . The effective Hamiltonian of such a driven valley-spin qubit can be written as follows [40]

$$\hat{H}_e = \frac{1}{2} g^* \mu_B \cdot B \cdot \hat{s} + \Omega_x \cos(\omega t) \hat{s}_x + \Omega_z \cos(\omega t) \hat{s}_z, \quad (A6)$$

where $\hat{s} = \{\hat{s}_x, \hat{s}_y, \hat{s}_z\}$ is the Pauli operator of a valley-spin qubit in the basis of the lower Kramers doublet $\{|\uparrow\rangle, |\downarrow\rangle\}$ with

$$|\uparrow\rangle = \cos(\zeta/2) |K'\rangle |\uparrow\rangle + \sin(\zeta/2) |K\rangle |\uparrow\rangle, \quad (A7)$$

$$|\downarrow\rangle = \sin(\zeta/2) |K'\rangle |\downarrow\rangle + \cos(\zeta/2) |K\rangle |\downarrow\rangle. \quad (A8)$$

The effective g tensor is

$$g^* = \begin{pmatrix} g_\perp & 0 & 0 \\ 0 & g_\perp & 0 \\ 0 & 0 & g_\parallel \end{pmatrix} \quad (A9)$$

with $g_\perp = g_s \sin \zeta$, $g_\parallel = g_s + 2g_{orb} \cos \zeta$. The effective driving Rabi frequencies are

$$\Omega_x = \sin(2\zeta) g_{orb} \mu_B B_z \delta\theta/2, \quad (A10)$$

$$\Omega_z = (2g_{orb} \cos \zeta + g_s \cos^2 \zeta) \mu_B B_x \delta\theta/2, \quad (A11)$$

with $\delta\theta = (\partial_z \theta)_{z=z_0} \Delta z_m$. Considering a magnetic field $B = \{B_x, 0, B_z\}$ in the x - z plane, the effective Hamiltonian can be written as

$$\hat{H}_e = \frac{1}{2} (\omega_x \hat{s}_x + \omega_z \hat{s}_z) + \Omega_x \cos(\omega t) \hat{s}_x + \Omega_z \cos(\omega t) \hat{s}_z \quad (A12)$$

where

$$\omega_x = g_\perp \mu_B B_x, \quad (A13)$$

$$\omega_z = g_\parallel \mu_B B_z. \quad (A14)$$

The eigenvalues of $\hat{H}_0 = \frac{1}{2} (\omega_x \hat{s}_x + \omega_z \hat{s}_z)$ are

$$\epsilon_{1,2} = \pm \sqrt{\omega_x^2 + \omega_z^2}/2, \quad (A15)$$

and the corresponding eigenstates are

$$|\psi_1\rangle = \cos(\gamma/2) |\uparrow\rangle + \sin(\gamma/2) |\downarrow\rangle, \quad (A16)$$

$$|\psi_2\rangle = -\sin(\gamma/2) |\uparrow\rangle + \cos(\gamma/2) |\downarrow\rangle \quad (A17)$$

with

$$\cos \gamma = \omega_z / \sqrt{\omega_x^2 + \omega_z^2}, \quad (A18)$$

$$\sin \gamma = \omega_x / \sqrt{\omega_x^2 + \omega_z^2}. \quad (A19)$$

We can rewrite the Hamiltonian \hat{H}_e in the basis of $\{|\psi_1\rangle, |\psi_2\rangle\}$ as follows

$$\hat{H}'_e = \frac{1}{2} \omega_0 \hat{S}_z + g_z \cos(\omega t) \hat{S}_z + g_x \cos(\omega t) \hat{S}_x \quad (A20)$$

with

$$\omega_0 = \sqrt{\omega_x^2 + \omega_z^2}, \quad (A21)$$

$$g_z = \Omega_z \cos \gamma + \Omega_x \sin \gamma, \quad (A22)$$

$$g_x = \Omega_x \cos \gamma - \Omega_z \sin \gamma, \quad (A23)$$

where \hat{S}_z and \hat{S}_x are Pauli matrices in the basis of $|\psi_1\rangle$ and $|\psi_2\rangle$. We choose $\omega = \omega_0$ and use rotating-wave approximation under the conditions $g_x, g_z \ll \omega_0$, which leads to a dressed valley-spin qubit system with the following effective Hamiltonian as

$$\hat{H}_d = \frac{1}{2} g_x \hat{S}_x. \quad (A24)$$

2. Coupling between a dressed valley-spin qubit and a local oscillating signal field

We first consider the situation in which a driven valley-spin qubit is coupled to a weak oscillating signal field $b = b \cos(\omega_c t) z$ in addition to the static magnetic field $B = \{B_x, 0, B_z\}$ with $|b| \ll |B|$. According to Eqs. A6-A12, the total Hamiltonian can be written as

$$\hat{H}_{eb} = \frac{1}{2} (\omega_x \hat{s}_x + \omega_z \hat{s}_z) + \Omega_x \cos(\omega t) \hat{s}_x + \Omega_z \cos(\omega t) \hat{s}_z + \Omega_c \cos(\omega_c t) \hat{s}_z, \quad (A25)$$

with $\Omega_c = g_\parallel \mu_B b/2$, where b only contributes to the first-order perturbative approximation of \hat{H} (Eq. A). The above Hamiltonian \hat{H}_{eb} can be written in the eigenbases of $\hat{H}_0 = \frac{1}{2} (\omega_x \hat{s}_x + \omega_z \hat{s}_z)$ as follows

$$\hat{H}'_{eb} = \frac{1}{2} \omega_0 \hat{S}_z + g_z \cos(\omega t) \hat{S}_z + g_x \cos(\omega t) \hat{S}_x + \Omega_c \cos \gamma \cos(\omega_c t) \hat{S}_z - \Omega_c \sin \gamma \cos(\omega_c t) \hat{S}_x. \quad (A26)$$

By choosing $\omega = \omega_0$ and using rotating-wave approximation under the conditions $\Omega_c \ll \omega_c$, $g_x, g_z \ll \omega_0$, we can obtain the following effective Hamiltonian for a dressed valley-spin qubit coupled to an oscillating magnetic field as

$$\hat{H}_{db} = \frac{1}{2} g_x \hat{S}_x + \Omega_c \cos(\omega_c t) \hat{S}_z, \quad (A27)$$

where we assume $\cos \gamma \approx 1$ that is valid when $\omega_x \ll \omega_z$.

3. Coupling between a dressed valley-spin qubit and a nuclear spin

We proceed to consider the situation in which a driven valley-spin qubit is coupled to a nuclear spin via magnetic dipole-dipole interaction. The interaction strength is usually

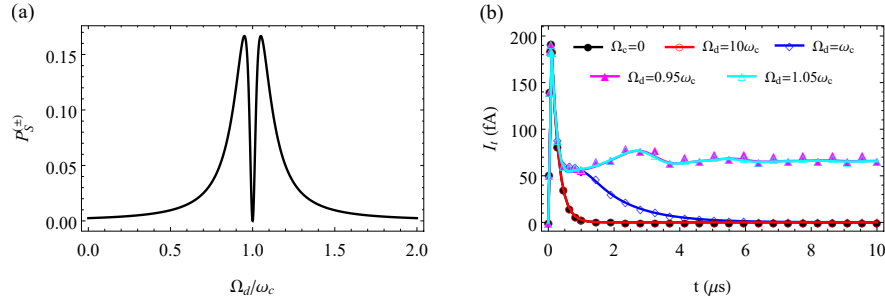


Fig.5. (Color online) (a) The average population of the singlet state $|S\rangle$ in the steady state as a function of the driving Rabi frequency Ω_d/ω_c . $P_S^{(\pm)}$ correspond to the initial state $|A_{\pm}\rangle$ respectively. (b) Leakage current I_t as a function of the evolution time t in the following situations: $\Omega_c = 0$ (no oscillating magnetic field), $\Omega_d = 10\omega_c$ (far detuning), $\Omega_d = \omega_c$ (on resonance), $\Omega_d = 0.95\omega_c$ and $\Omega_d = 1.05\omega_c$ (near resonance), with one unpolarised electron located in the right quantum dot as the initial state. The other parameters are $\omega_c = (2\pi) 5$ MHz, $\Omega_c = (2\pi) 0.5$ MHz, $\Gamma_L = \Gamma_R = (2\pi) 8$ MHz and $J = (2\pi) 2$ MHz.

much weaker than the static magnetic field $\mathbf{B} = \{B_x, 0, B_z\}$. The Hamiltonian of the total system is

$$\begin{aligned} \hat{H}_{en} = & \frac{1}{2} (\omega_x \hat{S}_x + \omega_z \hat{S}_z) + \Omega_x \cos(\omega t) \hat{S}_x + \Omega_z \cos(\omega t) \hat{S}_z \\ & + g_n \mu_N \mathbf{B} \cdot \hat{\mathbf{I}} + \left(\frac{\mu_0 \mu_B \mu_N}{4\pi r^3} \right) \left\{ (\mathbf{g}^* \cdot \hat{\mathbf{S}}/2) \cdot (g_n \hat{\mathbf{I}}) \right. \\ & \left. - 3 [(\mathbf{g}^* \cdot \hat{\mathbf{S}}/2) \cdot \mathbf{n}_r] \left[(g_n \hat{\mathbf{I}}) \cdot \mathbf{n}_r \right] \right\}, \end{aligned} \quad (\text{A28})$$

where g_n is the g factor of the nuclear spin, $\hat{\mathbf{I}} = \{\hat{I}_x, \hat{I}_y, \hat{I}_z\}$ is the spin operator of the nuclear spin and $\mathbf{r} = r\mathbf{n}_r$ is the vector connecting the valley-spin qubit and the nuclear spin with a distance r and a unit vector $\mathbf{n}_r = \{n_x, n_y, n_z\}$. Written in the eigenbases of \hat{H}_0 , one can obtain

$$\begin{aligned} \hat{H}'_{en} = & \frac{1}{2} \omega_0 \hat{S}_z + g_z \cos(\omega t) \hat{S}_z + g_x \cos(\omega t) \hat{S}_x + g_n \mu_N \mathbf{B} \cdot \hat{\mathbf{I}} \\ & + \left(\frac{\mu_0 \mu_B \mu_N g_n}{8\pi r^3} \right) \left\{ [g_{\perp} (\sin \gamma \hat{S}_z + \cos \gamma \hat{S}_x) \hat{I}_x + g_{\perp} \hat{S}_y \hat{I}_y \right. \\ & + g_{\parallel} (\cos \gamma \hat{S}_z - \sin \gamma \hat{S}_x) \hat{I}_z] - 3 [g_{\perp} n_x (\sin \gamma \hat{S}_z + \cos \gamma \hat{S}_x) \\ & + g_{\perp} n_y \hat{S}_y + g_{\parallel} n_z (\cos \gamma \hat{S}_z - \sin \gamma \hat{S}_x)] \\ & \left. (n_x \hat{I}_x + n_y \hat{I}_y + n_z \hat{I}_z) \right\}. \end{aligned} \quad (\text{A29})$$

Similarly, we choose $\omega = \omega_0$ and use rotating wave approximation under the conditions $g_x, g_z \ll \omega_0$ and $(\mu_0 \mu_B \mu_N g_n)/(8\pi r^3) \ll \omega_0 - (g_n \mu_N |\mathbf{B}|)$, thereby obtain the following effective Hamiltonian for a dressed valley-spin qubit coupled with a nuclear spin as described by

$$\begin{aligned} \hat{H}_{dn} = & \frac{1}{2} g_x \hat{S}_x + g_n \mu_N \mathbf{B} \cdot \hat{\mathbf{I}} + \frac{h_n}{2} [\hat{S}_z \hat{I}_z \\ & - 3 n_z \hat{S}_z (n_x \hat{I}_x + n_y \hat{I}_y + n_z \hat{I}_z)] \end{aligned} \quad (\text{A30})$$

with $h_n = \mu_0 \mu_B \mu_N g_n g_{\parallel}/(4\pi r^3)$, where we assume $\omega_x \ll \omega_z$ and thus $\cos \gamma \approx 1$. We remark that the above Hamiltonian can be straightforwardly generalised to the scenario of multiple nuclear spins.

Appendix B: Detailed mechanism of a nanotube quantum sensor

To illustrate the basic idea, here we present further details on the sensing mechanism for the detection of a weak oscillating magnetic field using a nanotube quantum sensor. The system dynamics is governed by the following quantum transport master equation as [55, 56]

$$\dot{\rho}_t = -i [\hat{\mathcal{H}}, \rho_t] + \mathcal{L} \rho_t, \quad (\text{B1})$$

with

$$\hat{\mathcal{H}} = \begin{pmatrix} \hat{\mathcal{H}}_I & 0 \\ 0 & \hat{\mathcal{H}}_{II} \end{pmatrix}, \quad (\text{B2})$$

where $\hat{\mathcal{H}}_I$ and $\hat{\mathcal{H}}_{II}$ correspond to the $(0, 1)$ and $(1, 1) \oplus (0, 2)$ subspaces respectively, namely

$$\hat{\mathcal{H}}_I = \frac{1}{2} \Omega_d \hat{S}_x^{(2)}, \quad (\text{B3})$$

and

$$\begin{aligned} \hat{\mathcal{H}}_{II} = & \frac{1}{2} \Omega_d \hat{S}_x^{(1)} + \Omega_c \cos(\omega_c t) \hat{S}_z^{(1)} + \frac{1}{2} \Omega_d \hat{S}_x^{(2)} \\ & + \Delta |S_g\rangle \langle S_g| + J (|S\rangle \langle S_g| + |S_g\rangle \langle S|), \end{aligned} \quad (\text{B4})$$

where $|S\rangle$ and $|S_g\rangle$ are the singlet states in $(1, 1)$ and $(0, 2)$ subspaces respectively. We note that $H_t = J (|S\rangle \langle S_g| + |S_g\rangle \langle S|)$ represents the tunneling between two quantum dots, and $H_{\Delta} = \Delta |S_g\rangle \langle S_g|$ is the Hamiltonian in the $(0, 2)$ subspace. The superoperator \mathcal{L} is generated by Lindblad operators $L_1 = \sqrt{\Gamma_L} \hat{a}_{1\psi}^{\dagger}$ and $L_2 = \sqrt{\Gamma_R} \hat{a}_{2\psi}$ describing the processes, by which an unpolarised electron is injected from the source at a rate Γ_L and is ejected to the drain at a rate Γ_R , where ψ denotes a set of complete and orthogonal basis states of a valley-spin qubit. The leakage current at time t can be calculated as follows

$$I(t) = (e\Gamma_R) \sum_{\psi} \text{Tr} \left(\hat{a}_{2\psi}^{\dagger} \hat{a}_{2\psi} \rho_t \right). \quad (\text{B5})$$

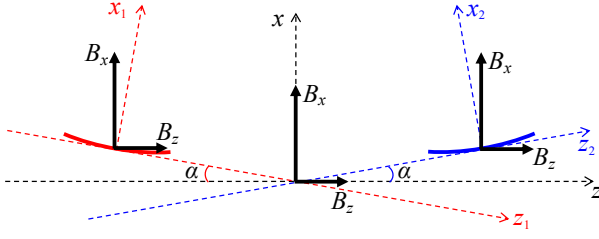


Fig.6. (Color online) Schematic diagram of coordinates for two quantum dots in a bent arc shape nanotube with a tilted angle α . Local coordinates x_1 - z_1 and coordinates x_2 - z_2 are used to describe the Hamiltonian of electron in the left and right quantum dot respectively. The magnetic field $B = B_x x + B_z z$ is applied in the x - z plane.

On the other hand, we derive the shot noise of the leakage current (see Eq.B5) as follows

$$\Delta I^2 = (e\Gamma_R)^2 \sum_{\psi} \left\{ \text{Tr} \left[\left(\hat{a}_{2\psi}^\dagger \hat{a}_{2\psi} \right)^2 \rho_t \right] - \left[\text{Tr} \left(\hat{a}_{2\psi}^\dagger \hat{a}_{2\psi} \rho_t \right) \right]^2 \right\}. \quad (\text{B6})$$

Therefore, the shot-noise limited measurement sensitivity for an evolution time t is given by

$$\eta = \Delta I \sqrt{t} / \left(\frac{\partial I}{\partial b} \right). \quad (\text{B7})$$

1. Tunnelling channels for leakage current

The system of a carbon nanotube double quantum dot in the $(1, 1)$ charge configuration can be described by the following Hamiltonian as

$$\hat{H}_{sb} = \frac{1}{2} \Omega_d \hat{S}_x^{(1)} + \Omega_c \cos(\omega_c t) \hat{S}_z^{(1)} + \frac{1}{2} \Omega_d \hat{S}_x^{(2)}, \quad (\text{B8})$$

where $g_x^{(1)} = g_x^{(2)} \equiv \Omega_d$ and $\hat{S}_{x,z}^{(j)}$ represent the Pauli operators of the left ($j = 1$) and right ($j = 2$) dressed valley-spin qubits. Here, we assume that both dressed valley-spin qubits are identical. We remark that two dressed valley-spin qubits may not be completely identical due to e.g. local disorder. We will address this issue in detail in the next section. Using rotating-wave approximation under the conditions $\Omega_c \ll \omega_c, \Omega_d$, in the interaction picture with respect to $\hat{H}_{sb}^{(0)} = (\omega_c/2) [\hat{S}_x^{(1)} + \hat{S}_x^{(2)}]$, the Hamiltonian \hat{H}_{sb} can be simplified into

$$\hat{H}'_{sb} = \frac{1}{2} \delta \hat{S}_z^{(1)} - \frac{1}{2} \Omega_c \hat{S}_x^{(1)} + \frac{1}{2} \delta \hat{S}_z^{(2)} \quad (\text{B9})$$

with $\delta = \Omega_d - \omega_c$, where we adopt a transformation $\hat{S}_x \leftrightarrow \hat{S}_z$ for simplicity and use rotating wave approximation. In the basis of $\{|A_0\rangle, |A_+\rangle, |A_-\rangle, |S\rangle\}$, one can partially diagonalize the Hamiltonian \hat{H}'_{sb} into the following form

$$\hat{H}''_{sb} = \begin{pmatrix} 0 & 0 & 0 & J_S^0 \\ 0 & \lambda/2 & 0 & J_S^+ \\ 0 & 0 & -\lambda/2 & J_S^- \\ J_S^0 & J_S^+ & J_S^- & 0 \end{pmatrix} \quad (\text{B10})$$

with $\lambda = \sqrt{4\delta^2 + \Omega_c^2}$, $J_S^0 = -\Omega_c^2/(2\lambda)$, $J_S^\pm = \delta\Omega_c/(\sqrt{2}\lambda)$, where

$$|A_0\rangle = \frac{1}{\sqrt{2}} \begin{pmatrix} \cos \vartheta \\ \sin \vartheta \\ \sin \vartheta \\ -\cos \vartheta \end{pmatrix}, \quad |A_\pm\rangle = \frac{1}{2} \begin{pmatrix} \pm 1 + \sin \vartheta \\ -\cos \vartheta \\ -\cos \vartheta \\ \pm 1 - \sin \vartheta \end{pmatrix} \quad (\text{B11})$$

with $\cos \vartheta = \Omega_c/\lambda$, $\sin \vartheta = 2\delta/\lambda$ and $|S\rangle = (1/\sqrt{2}) (0 \ -1 \ 1 \ 0)^T$ is the singlet state, which is the only unblocked state allowing electron tunnelling to the $(0, 2)$ -singlet state $|S_g\rangle$. The other three states $|A_0, \pm\rangle$ are blocked, nevertheless they couple with the singlet state $|S\rangle$ which may open three tunnelling channels for leakage current. The transitions $|A_0, \pm\rangle \leftrightarrow |S\rangle$ are characterised by the following reduced effective Hamiltonian as

$$\hat{H}_{A_0} = \begin{pmatrix} 0 & -\Omega_c^2/(2\lambda) \\ -\Omega_c^2/(2\lambda) & 0 \end{pmatrix}, \quad (\text{B12})$$

$$\hat{H}_{A_\pm} = \begin{pmatrix} \pm\lambda/2 & \delta\Omega_c/(\sqrt{2}\lambda) \\ \delta\Omega_c/(\sqrt{2}\lambda) & 0 \end{pmatrix}, \quad (\text{B13})$$

respectively. In the absence of a weak oscillating magnetic field (namely $\Omega_c = 0$), all of the channels to the state $|S\rangle$ are closed. In this case, the $|S\rangle$ state fraction leads to electron tunnelling and a prominent leakage current, see Fig.5(b). The other three states are blocked which results in exponentially decay of leakage current. The presence of the weak oscillating field would open three tunnelling channels via the transitions $|A_0, \pm\rangle \leftrightarrow |S\rangle$. To qualitatively understand the role of frequency detuning δ in these tunnelling channels, we assume that two electrons are initialised in the state $|A_0, \pm\rangle$ respectively. One can obtain that the average population of the singlet state $|S\rangle$ is

$$P_S^{(0)} = \frac{1}{2}, \quad (\text{B14})$$

$$P_S^{(\pm)} = \frac{4\delta^2 \Omega_c^2}{(4\delta^2 + \Omega_c^2)^2 + 8\delta^2 \Omega_c^2}. \quad (\text{B15})$$

For the transition $|A_0\rangle \leftrightarrow |S\rangle$, these two states $|S\rangle$ and $|A_0\rangle$ are on resonance, therefore the transition rate $\Omega_c^2/(2\lambda)$ is maximized when $\delta = 0$. In contrast, the transitions $|A_\pm\rangle \leftrightarrow |S\rangle$ rely on a non-zero frequency detuning, otherwise the transition rate $\delta\Omega_c/(\sqrt{2}\lambda)$ would instead be zero. Thus, these two tunnelling channels would make most significant contribution to leakage current with an appropriate non-zero frequency detuning. This is evident by two symmetric peaks in the average singlet state population when the initial states are $|A_\pm\rangle$, as shown in Fig.5(a). It can also be seen from Fig.5(b) that a small frequency detuning can sustain a relatively large leakage current in the steady state.

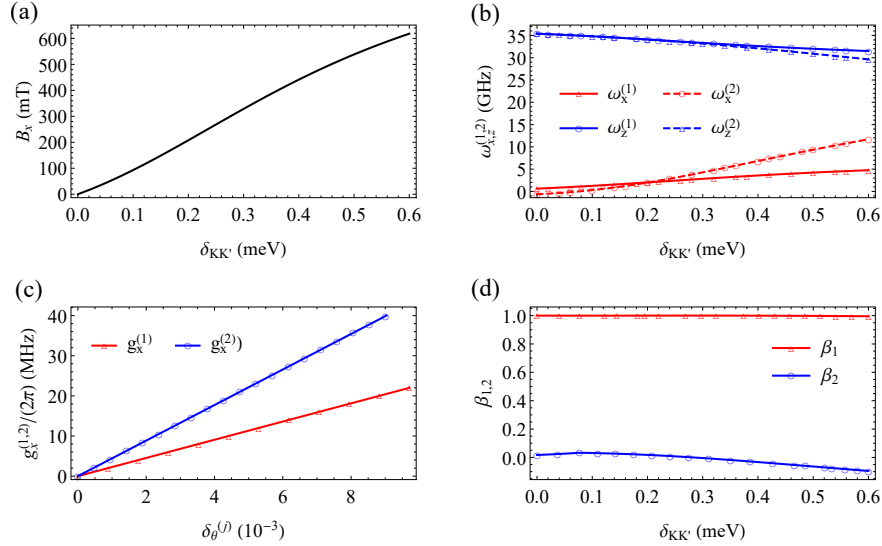


Fig.7. (Color online) The parameters to achieve the condition $\omega_0^{(1)} = \omega_0^{(2)}$ and $g_x^{(1)} = g_x^{(2)}$. (a) B_x as a function of the intervalley scattering difference $\delta_{KK'} = \Delta_{KK'}^{(2)} - \Delta_{KK'}^{(1)}$. (b) $\omega_{x,z}^{(1,2)}$ as a function of the intervalley scattering difference $\delta_{KK'}$. (c) For a certain value of $\delta_{KK'} = 0.2$ meV, $g_x^{(1,2)}$ as a function of the driving parameter $\delta_\theta^{(j)}$. (d) $\beta_{1,2}$ as a function of the intervalley scattering difference $\delta_{KK'}$. The other parameters are: $\Delta_{KK'}^{(1)} = 0.2$ meV, $\alpha = 1^\circ$, $B_z = 100$ mT.

2. Compensation of non-uniformity between two nanotube quantum dots

As the intervalley scattering is induced by electric disorder, it is usually hard to fabricate two valley-spin qubits that have uniform parameters. To be more specific, two nanotube quantum dots may have different valley mixing parameter $\Delta_{KK'}^{(j)}$ (see Eq.A4 and Eq.A6) which results in different values of the characteristic parameter ζ_j for two valley-spin qubits (see Eqs.A2-A5). In order to compensate such a non-uniformity, we consider a bent arc shape nanotube with an tilted angle α as shown in Fig.6. When applying a magnetic field in x - z plane, the magnetic fields for both electrons in the left ($j = 1$) and right ($j = 2$) nanotube quantum dot written in their local coordinates x_j - z_j are

$$B_{x_j}^{(j)} = B_x \cos \alpha + (-1)^{j+1} B_z \sin \alpha, \quad (\text{B16})$$

$$B_{z_j}^{(j)} = B_z \cos \alpha - (-1)^{j+1} B_x \sin \alpha. \quad (\text{B17})$$

The effective Hamiltonian of the driven valley-spin qubit in the left nanotube quantum dot, which interacts with an oscillating magnetic field, as written in its local coordinates x_1 - z_1 is

$$\begin{aligned} \hat{H}_{eb}^{(1)} = & \frac{1}{2} \left(\omega_{x_1}^{(1)} \hat{s}_{x_1}^{(1)} + \omega_{z_1}^{(1)} \hat{s}_{z_1}^{(1)} \right) + \Omega_{x_1}^{(1)} \cos(\omega t) \hat{s}_{x_1}^{(1)} \\ & + \Omega_{z_1}^{(1)} \cos(\omega t) \hat{s}_{z_1}^{(1)} + \Omega_c \cos(\omega_c t) \hat{s}_{z_1}^{(1)}, \end{aligned} \quad (\text{B18})$$

where $\delta_\theta^{(1)} = (\partial_{z_1} \theta_1)_{z_1=z_0} \Delta z_m^{(1)}$, $\omega_{x_1}^{(1)}$, $\omega_{z_1}^{(1)}$, $\Omega_{x_1}^{(1)}$, $\Omega_{z_1}^{(1)}$ are defined as in the Section S1-1, in which the parameter ζ_1 is given by $\tan \zeta_1 = \Delta_{KK'}^{(1)} / \Delta_{SO}^{(1)}$. The Pauli operators of the left valley-spin qubit $\hat{s}_{x_1}^{(1)}$, $\hat{s}_{y_1}^{(1)}$, $\hat{s}_{z_1}^{(1)}$ are defined in the following basis

as

$$|\uparrow_1^{(1)}\rangle = \cos(\zeta_1/2) |K'\rangle |\uparrow\rangle + \sin(\zeta_1/2) |K\rangle |\uparrow\rangle, \quad (\text{B19})$$

$$|\downarrow_1^{(1)}\rangle = \sin(\zeta_1/2) |K'\rangle |\downarrow\rangle + \cos(\zeta_1/2) |K\rangle |\downarrow\rangle. \quad (\text{B20})$$

Similarly, the effective Hamiltonian for the driven valley-spin qubit in the right nanotube quantum dot as written in its local coordinates x_2 - z_2 is

$$\begin{aligned} \hat{H}_e^{(2)} = & \frac{1}{2} \left(\omega_{x_2}^{(2)} \hat{s}_{x_2}^{(2)} + \omega_{z_2}^{(2)} \hat{s}_{z_2}^{(2)} \right) + \Omega_{x_2}^{(2)} \cos(\omega t) \hat{s}_{x_2}^{(2)} \\ & + \Omega_{z_2}^{(2)} \cos(\omega t) \hat{s}_{z_2}^{(2)} \end{aligned} \quad (\text{B21})$$

The corresponding Pauli operators $\hat{s}_{x_2}^{(2)}$, $\hat{s}_{y_2}^{(2)}$, $\hat{s}_{z_2}^{(2)}$ are written in the following basis as

$$|\uparrow_2^{(2)}\rangle = \cos(\zeta_2/2) |K'\rangle |\uparrow\rangle + \sin(\zeta_2/2) |K\rangle |\uparrow\rangle, \quad (\text{B22})$$

$$|\downarrow_2^{(2)}\rangle = \sin(\zeta_2/2) |K'\rangle |\downarrow\rangle + \cos(\zeta_2/2) |K\rangle |\downarrow\rangle, \quad (\text{B23})$$

with the characteristic parameter ζ_2 as defined by $\tan \zeta_2 = \Delta_{KK'}^{(2)} / \Delta_{SO}^{(2)}$. Therefore, the total effective Hamiltonian in the

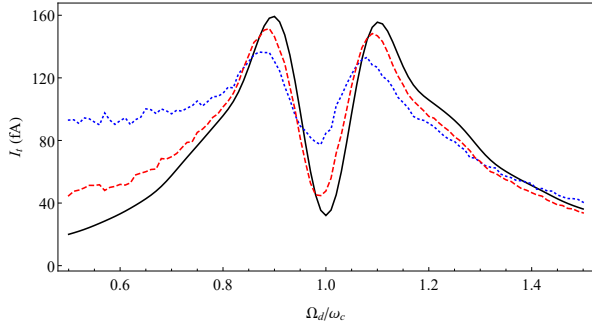


Fig.8. (Color online)(a)-(c) Leakage current I_t as a function of the driving Rabi frequency Ω_d/ω_c for an oscillating magnetic field with amplitude $b = 5.65 \mu\text{T}$ [$\Omega_c = (2\pi) 1 \text{ MHz}$] at time $t = 1.5 \mu\text{s}$, where solid, dashed, dotted lines represent the results simulated with $\Delta f = 0, 5, 10 \text{ MHz}$ and $\tau = 100 \text{ ms}$ respectively. The other parameters are the same as Figure.2 in the main text.

common coordinates x - z is

$$\begin{aligned}
 \hat{H}_{tb} &= \exp \left[-i\alpha \hat{s}_{y1}^{(1)} / 2 \right] \hat{H}_{eb}^{(1)} \exp \left[i\alpha \hat{s}_{y1}^{(1)} / 2 \right] \\
 &\quad + \exp \left[i\alpha \hat{s}_{y2}^{(2)} / 2 \right] \hat{H}_e^{(2)} \exp \left[-i\alpha \hat{s}_{y2}^{(2)} / 2 \right] \\
 &= \left[\cos \left(\frac{\alpha}{2} \right) - i\hat{s}_{y1}^{(1)} \sin \left(\frac{\alpha}{2} \right) \right] \hat{H}_{eb}^{(1)} \left[\cos \left(\frac{\alpha}{2} \right) + i\hat{s}_{y1}^{(1)} \sin \left(\frac{\alpha}{2} \right) \right] \\
 &\quad + \left[\cos \left(\frac{\alpha}{2} \right) + i\hat{s}_{y2}^{(2)} \sin \left(\frac{\alpha}{2} \right) \right] \hat{H}_e^{(2)} \left[\cos \left(\frac{\alpha}{2} \right) - i\hat{s}_{y2}^{(2)} \sin \left(\frac{\alpha}{2} \right) \right] \\
 &= \cos^2 \left(\frac{\alpha}{2} \right) \hat{H}_{eb}^{(1)} - i \sin \left(\frac{\alpha}{2} \right) \cos \left(\frac{\alpha}{2} \right) \hat{s}_{y1}^{(1)} \hat{H}_{eb}^{(1)} \\
 &\quad + i \sin \left(\frac{\alpha}{2} \right) \cos \left(\frac{\alpha}{2} \right) \hat{H}_{eb}^{(1)} \hat{s}_{y1}^{(1)} + \sin^2 \left(\frac{\alpha}{2} \right) \hat{s}_{y1}^{(1)} \hat{H}_{eb}^{(1)} \hat{s}_{y1}^{(1)} \\
 &\quad + \cos^2 \left(\frac{\alpha}{2} \right) \hat{H}_e^{(2)} + i \sin \left(\frac{\alpha}{2} \right) \cos \left(\frac{\alpha}{2} \right) \hat{s}_{y2}^{(2)} \hat{H}_e^{(2)} \\
 &\quad - i \sin \left(\frac{\alpha}{2} \right) \cos \left(\frac{\alpha}{2} \right) \hat{H}_e^{(2)} \hat{s}_{y2}^{(2)} + \sin^2 \left(\frac{\alpha}{2} \right) \hat{s}_{y2}^{(2)} \hat{H}_e^{(2)} \hat{s}_{y2}^{(2)} \\
 &= \frac{1}{2} \left(\omega_x^{(1)} \hat{s}_x^{(1)} + \omega_z^{(1)} \hat{s}_z^{(1)} \right) \\
 &\quad + \Omega_x^{(1)} \cos(\omega t) \hat{s}_x^{(1)} + \Omega_z^{(1)} \cos(\omega t) \hat{s}_z^{(1)} \\
 &\quad + \Omega_c \sin \alpha \cos(\omega_c t) \hat{s}_x^{(1)} + \Omega_c \cos \alpha \cos(\omega_c t) \hat{s}_z^{(1)} \\
 &\quad + \frac{1}{2} \left(\omega_x^{(2)} \hat{s}_x^{(2)} + \omega_z^{(2)} \hat{s}_z^{(2)} \right) + \Omega_x^{(2)} \cos(\omega t) \hat{s}_x^{(2)} \\
 &\quad + \Omega_z^{(2)} \cos(\omega t) \hat{s}_z^{(2)}
 \end{aligned} \tag{B24}$$

with

$$\omega_x^{(1)} = \omega_{x1}^{(1)} \cos \alpha + \omega_{z1}^{(1)} \sin \alpha, \tag{B25}$$

$$\omega_z^{(1)} = \omega_{z1}^{(1)} \cos \alpha - \omega_{x1}^{(1)} \sin \alpha, \tag{B26}$$

$$\Omega_x^{(1)} = \Omega_{x1}^{(1)} \cos \alpha + \Omega_{z1}^{(1)} \sin \alpha, \tag{B27}$$

$$\Omega_z^{(1)} = \Omega_{z1}^{(1)} \cos \alpha - \Omega_{x1}^{(1)} \sin \alpha, \tag{B28}$$

and

$$\omega_x^{(2)} = \omega_{x2}^{(2)} \cos \alpha - \omega_{z2}^{(2)} \sin \alpha, \tag{B29}$$

$$\omega_z^{(2)} = \omega_{z2}^{(2)} \cos \alpha + \omega_{x2}^{(2)} \sin \alpha, \tag{B30}$$

$$\Omega_x^{(2)} = \Omega_{x2}^{(2)} \cos \alpha - \Omega_{z2}^{(2)} \sin \alpha, \tag{B31}$$

$$\Omega_z^{(2)} = \Omega_{z2}^{(2)} \cos \alpha + \Omega_{x2}^{(2)} \sin \alpha. \tag{B32}$$

The Pauli matrices $\hat{s}_{x,z}^{(j)}$ are written in the following basis as

$$\begin{aligned}
 \left| \uparrow_j^{(j)} \right\rangle &= \exp \left[-(-1)^{j+1} i\alpha \hat{s}_{y_j}^{(j)} / 2 \right] \left| \uparrow_j^{(j)} \right\rangle \\
 &= \cos(\alpha/2) \left| \uparrow_j^{(j)} \right\rangle - (-1)^{j+1} i \sin(\alpha/2) \hat{s}_{y_j}^{(j)} \left| \uparrow_j^{(j)} \right\rangle \\
 &= \cos(\alpha/2) \left| \uparrow_j^{(j)} \right\rangle + (-1)^{j+1} \sin(\alpha/2) \left| \downarrow_j^{(j)} \right\rangle, \tag{B33}
 \end{aligned}$$

$$\begin{aligned}
 \left| \downarrow_j^{(j)} \right\rangle &= \exp \left[-(-1)^{j+1} i\alpha \hat{s}_{y_j}^{(j)} / 2 \right] \left| \downarrow_j^{(j)} \right\rangle \\
 &= \cos(\alpha/2) \left| \downarrow_j^{(j)} \right\rangle - (-1)^{j+1} i \sin(\alpha/2) \hat{s}_{y_j}^{(j)} \left| \downarrow_j^{(j)} \right\rangle \\
 &= \cos(\alpha/2) \left| \downarrow_j^{(j)} \right\rangle - (-1)^{j+1} \sin(\alpha/2) \left| \uparrow_j^{(j)} \right\rangle. \tag{B34}
 \end{aligned}$$

The eigenstates of $\hat{H}_0 = (1/2) \left[\omega_x^{(1)} \hat{s}_x^{(1)} + \omega_z^{(1)} \hat{s}_z^{(1)} \right] + (1/2) \left[\omega_x^{(2)} \hat{s}_x^{(2)} + \omega_z^{(2)} \hat{s}_z^{(2)} \right]$ are

$$|L_0\rangle = \cos(\gamma_1/2) \left| \uparrow^{(1)} \right\rangle + \sin(\gamma_1/2) \left| \downarrow^{(1)} \right\rangle, \tag{B35}$$

$$|L_1\rangle = -\sin(\gamma_1/2) \left| \uparrow^{(1)} \right\rangle + \cos(\gamma_1/2) \left| \downarrow^{(1)} \right\rangle, \tag{B36}$$

$$|R_0\rangle = \cos(\gamma_2/2) \left| \uparrow^{(2)} \right\rangle + \sin(\gamma_2/2) \left| \downarrow^{(2)} \right\rangle, \tag{B37}$$

$$|R_1\rangle = -\sin(\gamma_2/2) \left| \uparrow^{(2)} \right\rangle + \cos(\gamma_2/2) \left| \downarrow^{(2)} \right\rangle, \tag{B38}$$

with $\cos \gamma_j = \omega_z^{(j)} / \omega_0^{(j)}$ and $\sin \gamma_j = \omega_x^{(j)} / \omega_0^{(j)}$. In this set of bases, \hat{H}_{tb} can be rewritten by

$$\begin{aligned}
 \hat{H}'_{tb} &= \frac{1}{2} \omega_0^{(1)} \hat{s}_z^{(1)} + g_z^{(1)} \cos(\omega t) \hat{s}_z^{(1)} + g_x^{(1)} \cos(\omega t) \hat{s}_x^{(1)} \\
 &\quad + \Omega_{cz} \cos(\omega_c t) \hat{s}_z^{(1)} + \Omega_{cx} \cos(\omega_c t) \hat{s}_x^{(1)} + \frac{1}{2} \omega_0^{(2)} \hat{s}_z^{(2)} \\
 &\quad + g_z^{(2)} \cos(\omega t) \hat{s}_z^{(2)} + g_x^{(2)} \cos(\omega t) \hat{s}_x^{(2)}
 \end{aligned} \tag{B39}$$

with

$$\omega_0^{(j)} = \sqrt{\left(\omega_x^{(j)} \right)^2 + \left(\omega_z^{(j)} \right)^2}, \tag{B40}$$

$$g_z^{(j)} = \Omega_z^{(j)} \cos \gamma_j + \Omega_x^{(j)} \sin \gamma_j, \tag{B41}$$

$$g_x^{(j)} = \Omega_x^{(j)} \cos \gamma_j - \Omega_z^{(j)} \sin \gamma_j, \tag{B42}$$

$$\Omega_{cz} = \Omega_c \cos(\alpha - \gamma_1), \tag{B43}$$

$$\Omega_{cx} = \Omega_c \sin(\alpha - \gamma_1). \tag{B44}$$

In Fig.7(a), it can be seen that for a certain value of $\delta_{KK'}$, it is possible to satisfy the condition $\omega_0^{(1)} = \omega_0^{(2)}$ by choosing an appropriate magnetic field B_x . For example, one shall apply $B_x = 207 \text{ mT}$ for $\delta_{KK'} = 0.2 \text{ meV}$. And we plot the corresponding values of $\omega_{x,z}^{(j)}$ in Fig.7(b), which depend on

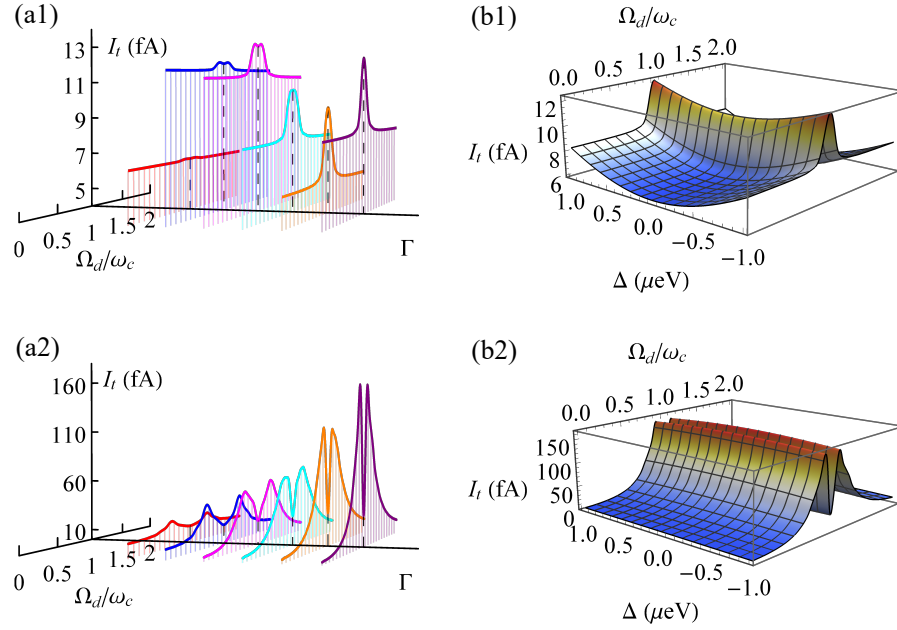


Fig.9. (Color online)(a1)-(a2) Leakage current I_t as a function of the driving Rabi frequency Ω_d/ω_c at time $t = 1.5 \mu\text{s}$ for an oscillating magnetic field with frequency $\omega_c = (2\pi) 5 \text{ MHz}$ and different amplitudes: (a1) $b = 0.565 \mu\text{T}$ [$\Omega_c = (2\pi) 0.1 \text{ MHz}$] simulated with $J = (2\pi) 10 \text{ MHz}$; (a2) $b = 5.65 \mu\text{T}$ [$\Omega_c = (2\pi) 1 \text{ MHz}$] simulated with $J = (2\pi) 20 \text{ MHz}$, in the presence of energy detuning $\Delta = 1 \mu\text{eV}$, where the red, blue, magenta, cyan, orange and purple lines represent the results simulated with the transition rate $\Gamma/(2\pi) = 10, 25, 75, 125, 250, 500 \text{ MHz}$ respectively. (b1)-(b2) Leakage current I_t as a function of the driving Rabi frequency Ω_d/ω_c and the energy detuning Δ at time $t = 1.5 \mu\text{s}$ for an oscillating magnetic field with frequency $\omega_c = (2\pi) 5 \text{ MHz}$ and different amplitudes: (b1) $b = 0.565 \mu\text{T}$ [$\Omega_c = (2\pi) 0.1 \text{ MHz}$] simulated with $J = (2\pi) 10 \text{ MHz}$; (b2) $b = 5.65 \mu\text{T}$ [$\Omega_c = (2\pi) 1 \text{ MHz}$] simulated with $J = (2\pi) 20 \text{ MHz}$. The injection and ejection rates are $\Gamma_L = \Gamma_R = \Gamma = (2\pi) 500 \text{ MHz}$.

$\delta_{KK'}$ and B_x . The driving Rabi frequencies $g_x^{(j)}$ depend on the driven motion parameter $\delta_\theta^{(j)}$, see Fig.7(c), which shows that $g_x^{(1)} = g_x^{(2)} = \Omega_d$ can be achieved by choosing appropriate $\delta_\theta^{(j)}$. Therefore, it is reasonable to consider the case of $\omega = \omega_0^{(1)} = \omega_0^{(2)}$. Using rotating-wave approximation under the conditions $\Omega_{cx}, \Omega_{cz} \ll \omega_c, g_x^{(j)}, g_z^{(j)} \ll \omega_0^{(j)}$, the total effective Hamiltonian can be simplified as follows

$$\hat{H}_{sb} = \frac{1}{2} \Omega_d \hat{S}_x^{(1)} + \Omega_c \cos(\omega_c t) \hat{S}_z^{(1)} + \frac{1}{2} \Omega_d \hat{S}_x^{(2)}, \quad (\text{B45})$$

where $\cos(\alpha - \gamma_1) \approx 1$ in the limit of $\omega_x^{(1)} \ll \omega_z^{(1)}$ and $\alpha \ll 1$.

Two electrons both in the right quantum dot can be considered as identical particles, thus the antisymmetric state can be written as

$$|S_g\rangle = \frac{1}{\sqrt{2}} (|R_1\rangle_2 |R_0\rangle_2 - |R_0\rangle_2 |R_1\rangle_2), \quad (\text{B46})$$

where the subscript 1 and 2 denotes the left and right quantum dot respectively. As the tunnelling between the left and right quantum dot would not change the electron state, the antisymmetric state of two electrons separated in the left and right quantum dot can be written as follows

$$|S\rangle = \frac{1}{\sqrt{2}} (|R_1\rangle_1 |R_0\rangle_2 - |R_0\rangle_1 |R_1\rangle_2). \quad (\text{B47})$$

Projecting Eq.B47 into the basis of $\{|L_0\rangle \otimes |R_0\rangle, |L_0\rangle \otimes |R_1\rangle, |L_1\rangle \otimes |R_0\rangle, |L_1\rangle \otimes |R_1\rangle\}$, one can obtain

$$|S\rangle = \frac{1}{\sqrt{2}} \beta_1 \cos[(\zeta_1 - \zeta_2)/2] (|L_1\rangle |R_0\rangle - |L_0\rangle |R_1\rangle) + \frac{1}{\sqrt{2}} \beta_2 \cos[(\zeta_1 - \zeta_2)/2] (|L_0\rangle |R_0\rangle + |L_1\rangle |R_1\rangle) \quad (\text{B48})$$

with

$$\langle L_0 | R_0 \rangle = \beta_1 \cos[(\zeta_1 - \zeta_2)/2], \quad (\text{B49})$$

$$\langle L_1 | R_1 \rangle = \beta_1 \cos[(\zeta_1 - \zeta_2)/2], \quad (\text{B50})$$

$$\langle L_0 | R_1 \rangle = \beta_2 \cos[(\zeta_1 - \zeta_2)/2], \quad (\text{B51})$$

$$\langle L_1 | R_0 \rangle = -\beta_2 \cos[(\zeta_1 - \zeta_2)/2], \quad (\text{B52})$$

and

$$\beta_1 = \cos[(\gamma_1 - \gamma_2)/2 + \alpha], \quad (\text{B53})$$

$$\beta_2 = \sin[(\gamma_1 - \gamma_2)/2 + \alpha]. \quad (\text{B54})$$

As shown in Fig.7(d), $\beta_2 \ll \beta_1$ is valid for a wide range of $\delta_{KK'}$ under the condition $\omega_0^{(1)} = \omega_0^{(2)}$. Therefore, after normalization, the antisymmetric state turns out to be

$$|S\rangle = \frac{1}{\sqrt{2}} (|L_1\rangle |R_0\rangle - |L_0\rangle |R_1\rangle). \quad (\text{B55})$$

Appendix C: Influence of decoherence

Gate-defined quantum dots in a carbon nanotube, suffers from decoherence mainly due to the hyperfine coupling with the environmental nuclear spins and the electric noise. The influence of nuclei may be mitigated by synthesizing carbon nanotube with isotopically purified $^{12}\text{CH}_4$, allowing for the fabrication of devices without nuclear spins [22]. Under ideal conditions, the coherence time of quantum dot in such a isotopically purified device is predicted to be of the order of seconds [47, 48]. However, the charge noise due to the electric potential fluctuations would modify the parameters of the quantum dot, namely inducing fluctuations of the energy difference Δ between the singlet states $|S\rangle$ and $|S_g\rangle$ [39], as $H_\Delta = \Delta |S_g\rangle \langle S_g|$. In this section, we provide detailed analysis of the influence of decoherence on our proposed carbon nanotube quantum sensor.

1. Hyperfine coupling with nuclei

Nanotubes synthesized from natural hydrocarbons consist of 99% ^{12}C (nuclear spin $I = 0$) and 1% ^{13}C (nuclear spin $I = \frac{1}{2}$). The abundance of ^{13}C nuclei may be reduced to 0.01% or even lower by using isotopically purified CH_4 during the growth of nanotubes. The hyperfine coupling to the ^{13}C nuclear spins induces magnetic field noise on the confined quantum dot, leading to the slow fluctuation of frequency detuning of the encoded valley-spin qubit. The effective Hamiltonian for detecting a weakly oscillating magnetic field in the (1, 1) charge configuration, incorporating the noise in frequency detunings $\delta\omega_i(t)$ ($i = 1, 2$), can be written as

$$\hat{H}_{sb}^* = \frac{1}{2} \left(\Omega_d \hat{S}_x^{(1)} + \delta\omega_1(t) \hat{S}_z^{(1)} \right) + \frac{1}{2} \left(\Omega_d \hat{S}_x^{(2)} + \delta\omega_2(t) \hat{S}_z^{(2)} \right) + \Omega_c \cos(\omega_c t) \hat{S}_z^{(1)} \quad (\text{C1})$$

For numerical simulation, we assume that $\delta\omega_i(t)$ ($i = 1, 2$) fulfills the Gaussian distribution

$$D(\delta\omega_i) = \frac{1}{\sqrt{2\pi}\Delta_f} e^{-\delta\omega_i^2/2\Delta_f^2}, \quad (\text{C2})$$

and evolves following the Ornstein-Uhlenbeck process with

$$\delta\omega_i(t + dt) = \delta\omega_i(t) e^{-dt/\tau} + \left[\Delta_f^2 \left(1 - e^{-2dt/\tau} \right) \right]^{1/2} n, \quad (\text{C3})$$

where τ is the correlation time which depends on the nuclear spin dynamics and relaxation, n represents a sample value of the unit normal random variable and $\Delta_f = \sqrt{2}/T_2^*$ is the standard deviation of $\delta\omega_i$. As T_2^* scales as $\sqrt{N/p}$ where N is the number of nuclei in the quantum dot and p is the isotopic fraction of ^{13}C we can estimate Δ_f from the upper limit of T_2^* that was measured in an 99% isotopically purified ^{13}C nanotube quantum dot with $N \approx 7 \times 10^4$ nuclei in the interaction range [46]. For an isotopic fraction of ^{13}C of 0.0127% and 0.05% percents we predict $\Delta_f = 5$ MHz and $\Delta_f = 10$ MHz respectively with the same value of N . As shown in

Figs.8, the fluctuation of frequency detuning induced by the hyperfine coupling would reduce the contrast of the resonance signal in a certain extent. Nevertheless, the influence can be well mitigated by isotopically engineering the nanotubes. The resonance signal of the oscillating magnetic field with larger amplitude demonstrates more robust feature. Similar results can be obtained in the case of nanoscale magnetic resonance spectroscopy.

2. Charge noise

As the carbon nanotube quantum dot is gate-defined, the electric noise would modify the energy levels of the quantum dot, i.e., inducing fluctuations of the energy detuning Δ between the singlet states $|S\rangle$ and $|S_g\rangle$ [39], as $H_\Delta = \Delta |S_g\rangle \langle S_g|$, the role of which in our scheme is mainly the suppression of effective tunneling. Thus, the influence may be compensated by choosing proper values of Γ_L , Γ_R and J . This is in contrast to the dephasing effect on the coherence time of qubit involving the singlet state $|S_g\rangle$ in the (0,2) subspace [33], where the energy splitting of the qubit relies on the energy detuning Δ .

As shown in Fig.9(a1)-(a2), when the energy detuning Δ up to $1\mu\text{eV}$ is considered, the resonant signal (dip or peak) of leakage current is degraded in the region with a small injection (ejection) rate of Γ ($\Gamma_L = \Gamma_R = \Gamma$). The influence of the energy detuning on the resonant signal becomes negligible for larger but still reasonable rates Γ (with $\Gamma_L = \Gamma_R = \Gamma$). The results hold without relying on a large amplitude of the oscillating magnetic field. In addition, the resonance signal of the leakage current is tolerant to the energy detuning varying from $-1\mu\text{eV}$ to $1\mu\text{eV}$ when the transition rate is chosen as $\Gamma/(2\pi) = 500$ MHz [39], see Fig.9(b1)-(b2). Therefore, improving the transition rate of the electron can efficiently compensate for the energy detuning between singlet states $|S\rangle$ and $|S_g\rangle$.

Appendix D: More details on the response of leakage current

1. Coupling to a weak oscillating signal field

As what we have presented in the main text, the leakage current always shows resonance features characterized by either a peak or a dip when the nanotube double quantum dot sensor couples with an oscillating magnetic field. The width of the resonance signal is critical for the spectra resolution. As shown in Fig.10(a1)-(a3), it can be seen that the frequency of an oscillating magnetic field can also influence the width of the resonance signal. In particular, a smaller ratio Ω_c/ω_c will lead to a sharper resonance signal.

In addition, there are another three important parameters Γ_L , J and Γ_R that are involved in the process of electron transport directly. Γ_L (Γ_R) determines the rate at which electrons are continuously pumped into (out of) the left (right) quantum dot. J represents the electron tunnelling rate between two quantum dots. Due to Coulomb blockade, these three parameters play an important role in the dynamic behaviour of the leakage

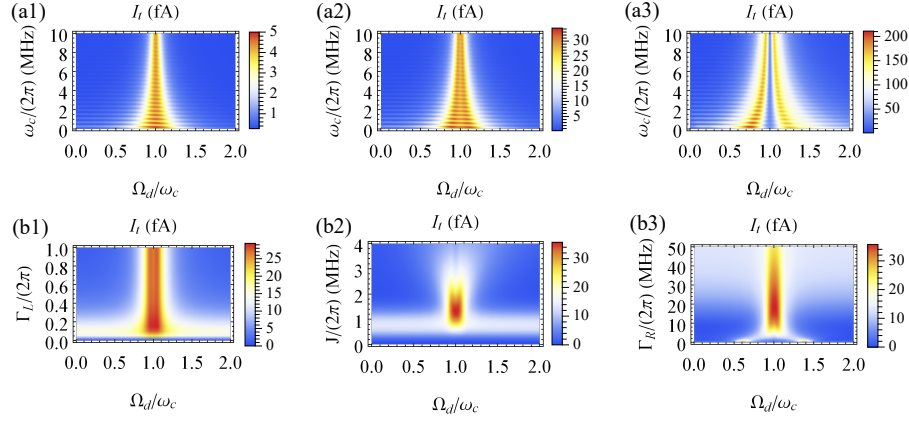


Fig.10. (Color online) (a1)-(a3) Leakage current I_t at time t as a function of the driving Rabi frequency Ω_d and the frequency ω_c of the oscillating magnetic field with different amplitudes: (a1) $b_z = 0.565 \mu\text{T}$ [$\Omega_c = (2\pi) 0.1$ MHz], (a2) $b_z = 1.70 \mu\text{T}$ [$\Omega_c = (2\pi) 0.3$ MHz], (a3) $b_z = 5.65 \mu\text{T}$ [$\Omega_c = (2\pi) 1$ MHz]. The other parameters are $J = (2\pi) 2$ MHz and $\Gamma_L = \Gamma_R = (2\pi) 8$ MHz. (b1) Leakage current I_t at time t as a function of the driving Rabi frequency Ω_d and the electron injection rate Γ_L with $\omega_c = (2\pi) 5$ MHz, $\Omega_c = (2\pi) 0.3$ MHz, $J = (2\pi) 2$ MHz and $\Gamma_R = (2\pi) 8$ MHz. (b2) Leakage current I_t at time t as a function of the driving Rabi frequency Ω_d and the tunnelling rate J with $\omega_c = (2\pi) 5$ MHz, $\Omega_c = (2\pi) 0.3$ MHz and $\Gamma_L = \Gamma_R = (2\pi) 8$ MHz. (b3) Leakage current at time t I_t as a function of the driving Rabi frequency Ω_d and the electron ejection rate Γ_R with $\omega_c = (2\pi) 5$ MHz, $\Omega_c = (2\pi) 0.3$ MHz, $J = (2\pi) 2$ MHz and $\Gamma_L = (2\pi) 8$ MHz. Taking one unpolarised electron located in the right quantum dot as the initial state. The time is set as $t = 1.5 \mu\text{s}$.

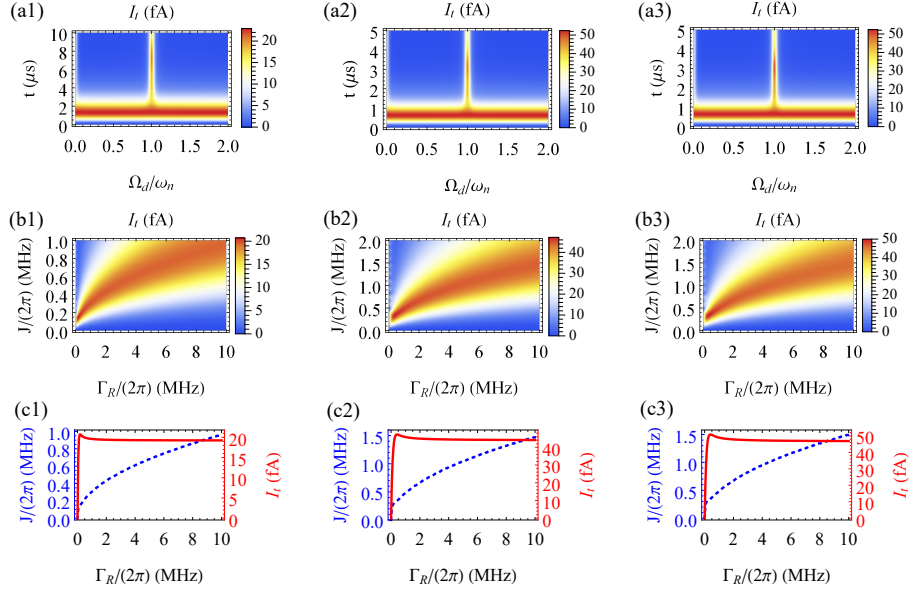


Fig.11. (Color online) (a1)-(a3) Leakage current I_t as a function of the driving Rabi frequency Ω_d/ω_n and the evolution time t for the nuclear spin ^{31}P (a1) with $\Gamma_R = (2\pi) 0.2$ MHz, $J = (2\pi) 0.15$ MHz; the nuclear spin ^{19}F (a2) with $\Gamma_R = (2\pi) 0.4$ MHz, $J = (2\pi) 0.35$ MHz; and the nuclear spin ^1H (a3) with $\Gamma_R = (2\pi) 0.4$ MHz, $J = (2\pi) 0.35$ MHz respectively, where $\omega_n = \gamma_n B$ is the Larmor frequency of nuclear spin. (b1)-(b3) Leakage current I_t as a function of the electron ejection rate Γ_R and the tunnelling rate J on resonance of the nuclear spin ^{31}P (b1) at time $t = 7 \mu\text{s}$, the nuclear spin ^{19}F (b2) at time $t = 5 \mu\text{s}$ and the nuclear spin ^1H (b3) at time $t = 3 \mu\text{s}$. (c1)-(c3) The optimised leakage current (red solid lines) and the optimal parameters (blue dashed lines) of the electron ejection rate Γ_R and the tunnelling rate J as shown in (b1)-(b3) respectively. In (a1)-(a3), (b1)-(b3), (c1)-(c3), the electron injection rate is $\Gamma_L = (2\pi) 1$ MHz, the magnetic field is $B_x = 300$ mT and $B_z = 100$ mT. The other parameters are the same as Fig.4 in the main text.

current when Pauli blockade is lifted by an oscillating magnetic field. As shown in Fig. 10(b1), the leakage current is saturated when the injection rate Γ_L becomes large, because the residual electrons in the source lead are (Coulomb) blocked by the electron in the left quantum dot. As shown in Fig. 10(b2)-

(b3), a large Γ_R and a suitable value of J would lead to a more prominent leakage current. The dependence of leakage current on these parameters may help to optimise the performance of the proposed nanotube quantum sensor.

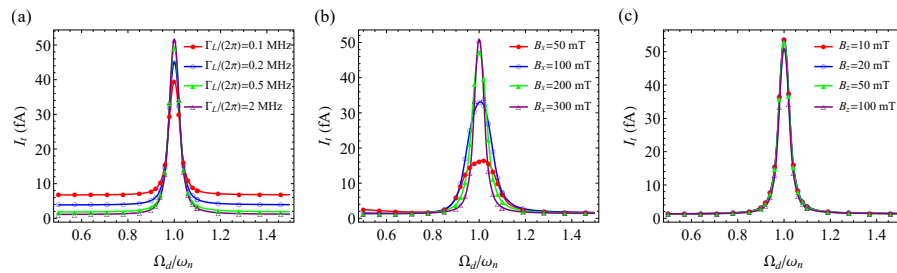


Fig.12. (Color online) Leakage current I_L as a function of the driving Rabi frequency Ω_d/ω_n for the nuclear spin ^1H , where $\omega_n = \gamma_n B$ is the Larmor frequency of nuclear spin. (a) under the situations with different injection rate Γ_L where $B_x = 300$ mT and $B_z = 100$ mT. (b) under the situations with different magnetic field B_x where $\Gamma_L = (2\pi) 1$ MHz and $B_z = 100$ mT. (c) under the situations with different magnetic field B_z where $\Gamma_L = (2\pi) 1$ MHz and $B_x = 300$ mT. In (a)-(c) $\Gamma_R = (2\pi) 0.4$ MHz, $J = (2\pi) 0.35$ MHz, and $t = 3 \mu\text{s}$. The other parameters are the same as Fig.4 in the main text.

2. Identifying nucleus species

Based on the essential idea for the detection of an oscillating field, we propose to realize single molecule detection in the main text. A single molecule is usually characterized by different species of nuclear spins with multiple Larmor frequencies. For each individual nuclear spin, the magnetic moment determines not only the Larmor frequency in an external magnetic field which indicates the driving Rabi frequency required to achieve a resonance signal but also the magnetic dipole-dipole coupling strength between the nuclear spin and the valley-spin qubit. As shown in Fig.11(a1)-(a3), once the driving Rabi frequency matches the Larmor frequency of each nuclear spin (^{31}P , ^{19}F , ^1H), the leakage current would demonstrate a resonance feature. Given the same distance between

the valley-spin qubit and the nuclear spin, the magnitude of leakage current induced by ^{31}P nuclear spin is much smaller than that of ^{31}F and ^1H nuclear spins due to its smaller magnetic moment. We remark that the values of parameters J and Γ_R have been optimised according to the results as shown in Fig.11(b1)-(b3).

We also investigate the effect of the parameters Γ_L , B_x , B_z on the observed resonance signal. In Fig.12(a), the leakage current on resonance increases with the electron injection rate Γ_L up to a saturation value when $\Gamma_L/2\pi$ is about 1 MHz. In Fig.12(b)-(c), we plot the leakage current for different values of transverse (B_x) and longitudinal (B_z) magnetic field components. It can be seen that the peak value of leakage current is almost independent on B_z , while it increases as B_x becomes larger.

-
- [1] C. L. Degen, F. Reinhard, and P. Cappellaro, *Rev. Mod. Phys.* **89**, 035002 (2017).
 - [2] A. M. Armani, R. P. Kulkarni, S. E. Fraser, R. C. Flagan, and K. J. Vahala, *Science* **317**, 783 (2007).
 - [3] J. O. Arroyo and P. Kukura, *Nature Photonics* **10**, 11 (2015).
 - [4] J. Lee, N. Tallarida, X. Chen, L. Jensen, and V. A. Apkarian, *Science Advances* **4** (2018).
 - [5] D. Glenn, D. Bucher, J. Lee, M. Lukin, H. Park, and R. Walsworth, *Nature* **555**, 351 (2018).
 - [6] S. Schmitt, T. Gefen, F. M. Stürner, T. Uden, G. Wolff, C. Müller, J. Scheuer, B. Naydenov, M. Markham, S. Pezzagna, *et al.*, *Science* **356**, 832 (2017).
 - [7] I. Lovchinsky, A. O. Sushkov, E. Urbach, N. P. de Leon, S. Choi, K. De Greve, R. Evans, R. Gertner, E. Bersin, C. Müller, L. McGuinness, F. Jelezko, R. L. Walsworth, H. Park, and M. D. Lukin, *Science* **351**, 836 (2016).
 - [8] F. Shi, Q. Zhang, P. Wang, H. Sun, J. Wang, X. Rong, M. Chen, C. Ju, F. Reinhard, H. Chen, J. Wrachtrup, J. Wang, and J. Du, *Science* **347**, 1135 (2015).
 - [9] C. Müller, X. Kong, J. M. Cai, K. Melentijević, A. Stacey, M. Markham, D. Twitchen, J. Isoya, S. Pezzagna, J. Meijer, J. F. Du, M. B. Plenio, B. Naydenov, L. P. McGuinness, and F. Jelezko, *Nature Communications* **5**, 4703 (2014).
 - [10] A. O. Sushkov, I. Lovchinsky, N. Chisholm, R. L. Walsworth, H. Park, and M. D. Lukin, *Phys. Rev. Lett.* **113**, 197601 (2014).
 - [11] T. Staudacher, F. Shi, S. Pezzagna, J. Meijer, J. Du, C. A. Meriles, F. Reinhard, and J. Wrachtrup, *Science* **339**, 561 (2013).
 - [12] H. J. Mamin, M. Kim, M. H. Sherwood, C. T. Rettner, K. Ohno, D. D. Awschalom, and D. Rugar, *Science* **339**, 557 (2013).
 - [13] J. Cai, F. Jelezko, and M. B. Plenio, *Nature Communications* **5**, 4065 (2014).
 - [14] T. Zhang, G.-Q. Liu, W.-H. Leong, C.-F. Liu, M.-H. Kwok, T. Ngai, R.-B. Liu, and Q. Li, *Nature Communications* **9**, 3188 (2018).
 - [15] M. W. Doherty, N. B. Manson, P. Delaney, F. Jelezko, J. Wrachtrup, and L. C. Hollenberg, *Physics Reports* **528**, 1 (2013).
 - [16] R. Schirhagl, K. Chang, M. Loretz, and C. L. Degen, *Annual Review of Physical Chemistry* **65**, 83 (2014).
 - [17] Y. Wu, F. Jelezko, M. B. Plenio, and T. Weil, *Angewandte Chemie International Edition* **55**, 6586 (2016).
 - [18] J. Tisler, G. Balasubramanian, B. Naydenov, R. Kolesov, B. Grotz, R. Reuter, J.-P. Boudou, P. A. Curmi, M. Sennour, A. Thorel, M. Börsch, K. Aulenbacher, R. Erdmann, P. R. Hemmer, F. Jelezko, and J. Wrachtrup, *ACS Nano* **3**, 1959 (2009).
 - [19] T. Rosskopf, A. Dussaux, K. Ohashi, M. Loretz, R. Schirhagl, H. Watanabe, S. Shikata, K. M. Itoh, and C. L. Degen, *Phys. Rev. Lett.* **112**, 147602 (2014).
 - [20] B. A. Myers, A. Das, M. C. Dartiailh, K. Ohno, D. D. Awschalom, and A. C. Bleszynski Jayich, *Phys. Rev. Lett.* **113**,

- 027602 (2014).
- [21] M. Kim, H. J. Mamin, M. H. Sherwood, K. Ohno, D. D. Awschalom, and D. Rugar, *Phys. Rev. Lett.* **115**, 087602 (2015).
 - [22] E. A. Laird, F. Kuemmeth, G. A. Steele, K. Grove-Rasmussen, J. Nygård, K. Flensberg, and L. P. Kouwenhoven, *Rev. Mod. Phys.* **87**, 703 (2015).
 - [23] N. Rohling and G. Burkard, *New Journal of Physics* **14**, 083008 (2012).
 - [24] A. Pályi and G. Burkard, *Phys. Rev. B* **80**, 201404 (2009).
 - [25] S. J. Chorley, G. Giavaras, J. Wabnig, G. A. C. Jones, C. G. Smith, G. A. D. Briggs, and M. R. Buitelaar, *Phys. Rev. Lett.* **106**, 206801 (2011).
 - [26] H. O. H. Churchill, F. Kuemmeth, J. W. Harlow, A. J. Bestwick, E. I. Rashba, K. Flensberg, C. H. Stwertka, T. Taychatanapat, S. K. Watson, and C. M. Marcus, *Phys. Rev. Lett.* **102**, 166802 (2009).
 - [27] F. Pei, E. A. Laird, G. A. Steele, and L. P. Kouwenhoven, *Nature Nanotechnology* **7**, 630 (2012).
 - [28] S. Moriyama, T. Fuse, M. Suzuki, Y. Aoyagi, and K. Ishibashi, *Phys. Rev. Lett.* **94**, 186806 (2005).
 - [29] K. Grove-Rasmussen, S. Grap, J. Paaske, K. Flensberg, S. Andergassen, V. Meden, H. I. Jørgensen, K. Muraki, and T. Fujisawa, *Phys. Rev. Lett.* **108**, 176802 (2012).
 - [30] F. H. L. Koppens, C. Buizert, K. J. Tielrooij, I. T. Vink, K. C. Nowack, T. Meunier, L. P. Kouwenhoven, and L. M. K. Vandersypen, *Nature* **442**, 766 (2006).
 - [31] S. Thiele, F. Balestro, R. Ballou, S. Klyatskaya, M. Ruben, and W. Wernsdorfer, *Science* **344**, 1135 (2014).
 - [32] K. Flensberg and C. M. Marcus, *Phys. Rev. B* **81**, 195418 (2010).
 - [33] E. A. Laird, F. Pei, and L. P. Kouwenhoven, *Nature Nanotechnology* **8**, 565 (2013).
 - [34] F. H. L. Koppens, J. A. Folk, J. M. Elzerman, R. Hanson, L. H. W. van Beveren, I. T. Vink, H. P. Tranitz, W. Wegscheider, L. P. Kouwenhoven, and L. M. K. Vandersypen, *Science* **309**, 1346 (2005).
 - [35] O. N. Jouravlev and Y. V. Nazarov, *Phys. Rev. Lett.* **96**, 176804 (2006).
 - [36] K. Grove-Rasmussen, H. I. Jørgensen, T. Hayashi, P. E. Lindelof, and T. Fujisawa, *Nano Letters* **8**, 1055 (2008).
 - [37] J. P. Lu, *Phys. Rev. Lett.* **74**, 1123 (1995).
 - [38] G. Széchenyi and A. Pályi, *Phys. Rev. B* **91**, 045431 (2015).
 - [39] G. Széchenyi and A. Pályi, *Phys. Rev. B* **95**, 035431 (2017).
 - [40] Y. Li, S. C. Benjamin, G. A. D. Briggs, and E. A. Laird, *Phys. Rev. B* **90**, 195440 (2014).
 - [41] F. Kuemmeth, S. Ilani, D. C. Ralph, and P. L. McEuen, *Nature* **452**, 448 (2008).
 - [42] A. Pályi and G. Burkard, *Phys. Rev. B* **82**, 155424 (2010).
 - [43] M. C. Hels, B. Braunecker, K. Grove-Rasmussen, and J. Nygård, *Phys. Rev. Lett.* **117**, 276802 (2016).
 - [44] J.-M. Cai, B. Naydenov, R. Pfeiffer, L. P. McGuinness, K. D. Jahnke, F. Jelezko, M. B. Plenio, and A. Retzker, *New Journal of Physics* **14**, 113023 (2012).
 - [45] R. Hanson, L. P. Kouwenhoven, J. R. Petta, S. Tarucha, and L. M. K. Vandersypen, *Rev. Mod. Phys.* **79**, 1217 (2007).
 - [46] H. O. H. Churchill, F. Kuemmeth, J. W. Harlow, A. J. Bestwick, E. I. Rashba, K. Flensberg, C. H. Stwertka, T. Taychatanapat, S. K. Watson, and C. M. Marcus, *Phys. Rev. Lett.* **102**, 166802 (2009).
 - [47] D. V. Bulaev, B. Trauzettel, and D. Loss, *Phys. Rev. B* **77**, 235301 (2008).
 - [48] M. S. Rudner and E. I. Rashba, *Phys. Rev. B* **81**, 125426 (2010).
 - [49] B. M. Freeman, J. S. Schoenfield, and H. Jiang, *Applied Physics Letters* **108**, 253108 (2016).
 - [50] W. A. Coish and F. Qassemi, *Phys. Rev. B* **84**, 245407 (2011).
 - [51] N. S. Lai, W. H. Lim, C. H. Yang, F. A. Zwanenburg, W. A. Coish, F. Qassemi, A. Morello, and A. S. Dzurak, *Scientific Reports* **1**, 110 (2011).
 - [52] R. Hanson, L. M. K. Vandersypen, L. H. W. van Beveren, J. M. Elzerman, I. T. Vink, and L. P. Kouwenhoven, *Phys. Rev. B* **70**, 241304 (2004).
 - [53] X. Tu and M. Zheng, *Nano Research* **1**, 185 (2008).
 - [54] H. K. Moon, C. I. Chang, D.-K. Lee, and H. C. Choi, *Nano Research* **1**, 351 (2008).
 - [55] S. A. Gurvitz and Y. S. Prager, *Phys. Rev. B* **53**, 15932 (1996).
 - [56] X.-Q. Li, J. Luo, Y.-G. Yang, P. Cui, and Y. Yan, *Phys. Rev. B* **71**, 205304 (2005).